Characterization of Local Deformation in Pb-free Solder Joints

Using Three Dimensional (3D) X-ray Microtomography

by

Eric Padilla

A Thesis Presented in Partial Fulfillment
of the Requirements for the Degree
Master of Science

Approved April 2012 by the
Graduate Supervisory Committee:

Nikhilesh Chawla, Chair
Terry Alford
Stephen Krause

ARIZONA STATE UNIVERSITY

May 2012

ABSTRACT

Pb-free solder joints are commonly used as interconnects in semiconductor packaging. One of the major defects affecting the mechanical performance of solder joints are reflow pores that form during processing. These pores exhibit significant variability in size and distribution, and understanding the effects of pore geometry on failure is an important reliability concern. In this thesis, the pore microstructures of solder joint samples and the localized plastic deformation around individual pores was characterized in 3D using lab scale X-ray Microtomography.

To observe the deformation of a solder joint in 3D, a solder joint was imaged with Microtomography after reflow and then deformed in shear in several loading steps with additional tomography data taken between each. The 3D tomography datasets were then segmented using the 3D Livewire technique into regions corresponding to solder and pores, and used to generate 3D models of the joint at each strain value using Mimics software. The extent of deformation of individual pores in the joint as a function of strain was quantified using sphericity measurements, and correlated with the observed cracking in the joint. In addition, the error inherent in the data acquisition and 3D modeling process was also quantified.

The progression of damage observed with X-ray Microtomography was then used to validate the deformation and failure predicted by a Finite Element (FE) simulation. The FE model was based on the as-reflowed tomography data, and incorporated a ductile damage failure model to simulate fracture. Using the

measured sphericity change and cracking information obtained from the tomography data, the FE model is shown to correctly capture the broad plastic deformation and strain localization seen in the actual joint, as well as the crack propagation.

Lastly, Digital Image Correlation was investigated as a method of obtaining improved local strain measurements in 3D. This technique measures the displacement of the inherent microstructural features of the joint, and can give localized strain measurements that can be directly comparable to that predicted by modeling. The technique is demonstrated in 2D on Pb-Sn solder, and example 3D data is presented for future analysis.

ACKNOWLEDGMENTS

I am very appreciative of the individuals who allowed me the opportunity to work on this research. I thank my advisor, Dr. Nikhilesh Chawla for his guidance and wisdom, and am grateful for the opportunity to work in his group. I sincerely thank Dr. Terry Alford and Dr. Stephen Krause for their support. Through the Semiconductor Research Corporation, I was able to work with Dr. Mario Pacheco of Intel Corporation very regularly on this project, and I am very grateful for his constant guidance and perspective, and his generosity with his time and Tomography equipment. Likewise, I am grateful to Dr. Ravi Mahajan and Dr. Joseph Cianfrone of Intel for their support and assistance. I also would like to acknowledge the Semiconductor Research Corporation Education Alliance and Intel Corporation, who funded my graduate study.

I would not be here without the help from many friends and colleagues, and I sincerely thank each and every one of my lab-mates, who have all been there to help in a bind. Specifically I would like to acknowledge Vaidehi Jakkali, who did the Finite Element modeling discussed herein. In addition, I am eternally grateful to my friends at the UCLA Center for Excellence and Diversity, and Dani Napier-Harrison and Shirley Maier for giving me the tools to both afford and succeed in grad school.

Lastly, I would like to thank my family, especially Nichole, for their ever-present love and support.

TABLE OF CONTENTS

Page

CHAPTER Page

LIST OF TABLES

LIST OF FIGURES

Figure Page

Chapter 1

INTRODUCTION

1.1 Introduction

Pb-free solder joints are commonly used to form mechanical and electrical connections between levels in electronic packages. In a typical semiconductor package, solder joints are used for C4 flip chip connections and BGA arrays, amounting to several hundred joints in a package. As device and interconnect sizes decrease, managing microstructural defects becomes increasingly important for ensuring reliability. A common cause of premature failure in metallic interconnects is the presence of porosity. In Sn-rich solder, porosity formed during reflow is a common defect which is difficult to eliminate, and can cause a significant degradation of the joint's mechanical properties. These pores typically come from entrapment of gaseous flux and air during cooling (Lau and Eramus 2002) (Aspandiar 2005), and have been shown to decrease joint electrical conductivity (Yunus, et al. 2003), thermal conductivity (Zhu 1999), and fatigue life (Yu, et al. 2008).

In order to capture the microstructural features within a material in 3D, a number of techniques can be used. One of the most common is serial sectioning microscopy (Sindhu and Chawla 2004), (Dudek and Chawla, Three-dimensional (3D) Microstructure Visualization of LaSn3 Intermetallics in a Novel Sn-rich Rare-earth-containing Solder 2008), where a surface is repeatedly polished and then imaged, producing cross sectional images though the sample. This can be done by hand or with a Focused Ion Beam/SEM through a process termed FIB

tomography (Kubis, Shiflet and Hull 2004) (Singh and Chawla 2010). While serial sectioning allows high resolution microstructural imaging, it unfortunately destroys the sample. For experiments on microstructural evolution, imaging a specimen non-destructively is much more useful, since the same specimen can be imaged before and after processing, yielding four-dimensional (4D) material data. This allows limited microstructural evolution analysis (Lasagni, et al. 2007), but the destructive nature of serial sectioning, precludes any true 4D analysis. X-ray Computed Tomography (CT) is an excellent technique to quantify microstructures non-destructively. X-ray Microtomography imaging tools with resolution limits around 1 μm have been developed with synchrotron (Williams, et al. 2010) (Baruchel, Bleuet, et al. 2008) (Baruchel, Buffière, et al. 2006) (Kinney and Nichols 1992) as well as lab-scale x-ray sources (Wang, et al. 2004) (Stock 2008)). The non-destructive nature of this technique enables us to track the complex 3D changes in the microstructure over time, and the deformation in the material can be quantified on a local level and be directly compared to computer simulation. X-ray tomography is an excellent tool for this analysis because not only does it provide a microstructurally realistic input to modeling (Dudek, Hunter, et al. 2010), but it allows validation of those models by comparison to experimental observation.

1.2 Literature Review

The demand for environmentally friendly materials and smaller feature sizes in semiconductor packaging has led to the widespread use of Sn-rich Pb free

interconnects. As feature sizes decrease, microstructural defects within solder joints have a larger influence on their thermal and mechanical behavior (Plieninger, Dittes and Pressel 2006). The effect of pores on thermo-mechanical behavior of solder has been studied by a number of authors. Yunus (Yunus, et al. 2003) experimentally observed that voids larger than 50% of 2d cross sectional area cause significant reductions in sample lifetime during torsion testing. Lau and Erasmus (Lau and Eramus 2002) used Finite Element (FE) analysis to determine that solder creep in BCC++ joints increased with void size, but that pores below 20% volume fraction didn't pose a reliability concern. Ladani and Dasgupta (Ladani and Dasgupta 2007) found that durability started to decrease within joints when porosity increased above 15%, also using FEM modeling. Both of these groups found that the position of pores within the FE model affected the joint strength, with pores near the corners of the joint at the Solder/pad interface having the highest effect on strength. One of the shortcomings of many studies on modeling of solder porosity is that an oversimplified system is used to represent the real joint. Often models contain a small number of perfectly spherical pores, when real joints can contain over a hundred pores of a variety of sizes. The interaction between pores also plays a significant role in deformation. Yunus et al. (Yunus, et al. 2003) for example show that small voids in general do not reduce fatigue lifetime, but when clustered together near the crack path, can link up during fracture. Additionally, Xu (Xu, Wen and Zhai 2011) showed that when pores are spaced less than one radius apart perpendicular to the loading direction, stress amplification occurs in between the pores. The complex stress

state throughout a real joint cannot be modeled accurately with a simple model, but instead should include as many microstructurally realistic features as possible. In order to create such a model, the microstructure of a joint must be accurately imaged and reconstructed in 3D. Furthermore, incorporating a realistic microstructure into a damage prediction model allows the opportunity to experimentally verify the results, increasing confidence in the model's output.

X-ray tomography has been used as a basis for obtaining microstructurally realistic Finite Element models in other material systems. Specifically, the detrimental effects of porosity have been examined in several metallic systems. Nicoletto et al. (Nicoletto, Konecnia and Fintova 2012 (in press)) simulated the stress concentration around individual casting pores Al-Si, improving on previous spherical-pore approximation models. Vanderesse et al. (Vanderesse, et al. 2011) incorporated realistic casting pore microstructures into an elastic FE model to predict stress fields around pores. Weck et al. (Weck, et al. 2008) looked at the plasticity and coalescence of artificially created voids in copper using in-situ tensile testing in a tomography setup, and compared the results with a number of void growth models. Li et al. (Li, et al. 2006) conducted a 4D study, where a cast Al specimen was imaged with tomography before and after fatigue cycling. Using an elastic-plastic model that incorporates the casting porosity, they showed that an area of initially high stress localization due to porosity eventually develops a fatigue crack after cycling. Similarly Youssef et al. (Youssef, Maire and Gaertner 2005) showed qualitative comparisons of pore shape changes in a metallic foam, by x-ray tomography experiments and FE simulations.

What is lacking in previous work, however, is Finite Element models that predict the onset and evolution of plasticity and fracture due to porosity. Furthermore, very little work has been done on coupling x-ray tomography data with microstructure-based finite element modeling to verify that the simulated result is accurate.

Because the pores within the solder are the main microstructural feature that in resolvable in lab scale tomography, observing their deformation is the best method of quantifying the deformation in the joint. Several authors have quantified the shape and size changes in pores and other phases using X-ray tomography data. The simplest analysis of this type is to measure the volume change of the phase of interest. Tian et. al. (Tian, et al. 2011) measured the void volume change due to electromigration in a SnPb solder joint, and Martin et. al (Martin, et al. 2000) coupled an increase in cavity volume with a decrease in cavity count to obtain an interlinkage parameter to measure coalescence. Landron et al. (Landron, et al. 2011) and Maire et al. (Maire, et al. 2011) measure void growth of pores in steels and Al alloys respectively. Maire establishes that since the absolute error is on the order of one voxel, the relative error is highly dependent on cavity size. Both studies plot volume change in terms of equivalent size, which is described below. The equivalent size change of entire populations of pores is given as a function of strain in both studies, while Maire et al. discusses that tracking individual pores from one dataset to the next is difficult, but is able to show data showing the void growth of a handful of individual cavities.

While size change is a useful characterization tool to study pores, it does not give any information on the shape change associated with processing. When considering shape, there are several parameters that have been used for different applications, such as the flatness and elongation of best-fit ellipses to characterize phase morphology (Cao, Pourbabak and Schryvers 2012) and curvature to characterize interfacial shape during casting. (Felberbaum and Rappaz 2011) For more general shape characterization, several authors have used Sphericity (or Circularity in 2D) to compare phase morphology between samples (Lange, Jennings and Shah 1994), (Weiler, et al. 2005) (Lasagni, et al. 2007). Link et al. (Link, et al. 2006) expanded beyond this, and used sphericity first to filter out ring-artifacts from tomography data, and then showed the aggregate sphericity distribution of pores in Ni-based superalloys. They observed a sphericity decrease during creep, and used it to quantify the transformation from nearly spherical pores in the undeformed specimen to polyhedral pores after creep. This characterization is able to quantify the changes in the pores as a group, but like the studies above, doesn't give information about individual pores. This type of analysis doesn't work well in the situation where a significant amount of strain localization is observed, as pores in different regions of the sample can exhibit significantly different behavior. Instead, sphericity measurements on individual pores will be conducted to show local behavior.

1.3 Focus of the Thesis

The focus of this thesis is the characterization of experimentally observed deformation in 3D, which can greatly benefit from analysis techniques that incorporate the nondestructive imaging allowed by X-ray Microtomography. These 3D characterization techniques are applied to Sn-3.9Ag-0.7Cu lap shear solder joints in order to understand the effects of solder pore size, shape and distribution on joint deformation and failure. By being able to accurately image sample microstructures in 3D, failure analysis is able to move beyond probabilistic testing and idealized simulation and allows characterization of the deformation and failure behavior of a specific sample using its own unique microstructural features. In Chapter 2, X-ray tomography is used to obtain 3D imagery of a solder joint at several stages of deformation. The data is then segmented into regions corresponding to solder and porosity, and the techniques used to obtain accurate microstructural reconstructions are discussed. Specifically, the Livewire algorithm is demonstrated to produce repeatable segmentations with low sensitivity to user inputs and image artifacts, making it an excellent choice for this application. The local state of deformation in the joint is characterized by taking advantage of the high contrast between porosity in the joint and the solder, allowing quantification of the pore shape change as a function of time. By measuring the sphericity of individual pores at each strain value, the decrease in sphericity can be used to quantify the local deformation at that point, and the sphericity decrease behavior for pores in different regions of the joint can be correlated with the observed fracture. In Chapter 3, the error involved in the

acquisition and modeling process is quantified, and in Chapter 4, the sphericity analysis is used to validate a Finite Element model designed to predict the deformation and failure behavior in the joint. The sphericity decrease is shown to be similar for the FE model and experimental data for several pores. This data is also compared to the sphericity decrease predicted by simple shear of the zero-strain pores, as modeled in MATLAB. The X-ray tomography data is also used to validate the model's prediction of the crack initiation and propagation path in the joint. In Chapter 5, Digital Volume Correlation is discussed as a technique to obtain localized measurements of strain within a joint using the native features of a sample's microstructure as imaged with X-ray tomography. This technique is difficult to implement with lab-scale tomography data, but is very promising as an avenue for obtaining 3D strain measurements in the future.

Chapter 2

QUANTIFYING LOCAL PORE DEFORMATION DUE TO SHEAR STRAIN IN A PB-FREE SOLDER JOINT

2.1 Introduction:

X-ray microtomography has been used as a failure analysis tool for semiconductor packaging (Pacheco and Goyal 2008), and labscale tomography tools can nondestructively image relatively large solder joints (~1mm) with resolutions of 2 um. Tomography works well for this analysis, since it can clearly resolve pores in the joint down to about 10 um in diameter, which encompasses the majority of porosity in the joint. A typical tomography cross section for a solder joint shows the solder as a homogenous phase, the Cu pads, and the included pores within the joint (Figure 1). In this experiment, the solder joint is deformed in simple shear, which causes pore elongation to occur primarily in the loading direction. This elongation should likewise be predicted by a failure prediction model incorporating the plastic deformation in the joint. By characterizing the resulting shape change of individual pores upon physical loading, the extent of deformation around each pore can be quantified and compared to the corresponding changes predicted by the finite element model.

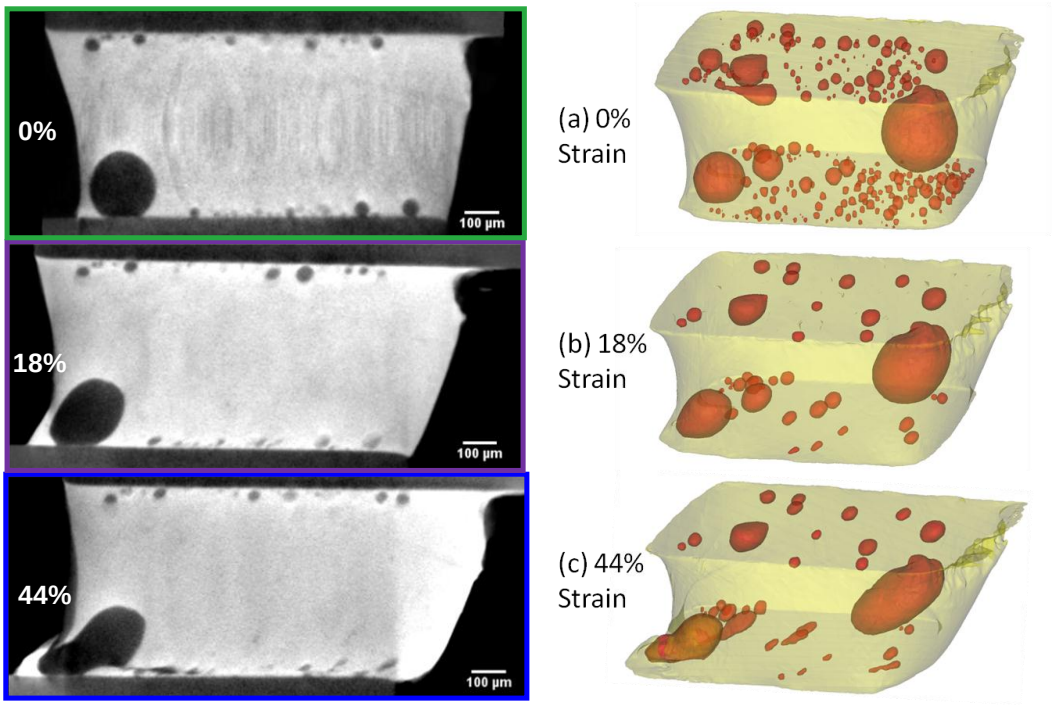

Figure 1: (a): Cross sections of a similar plane though the solder joint at indicated shear strains. (b): 3D reconstructions of tomography data showing solder (yellow) and reflow pores (red). At 18% and 44% strain, only selected pores are shown

2.2 Sample Preparation

A single-lap shear joint of Sn-3.9Ag-0.7Cu alloy was reflowed between two copper bars. To prepare the joint, a 1 x 1 mm square was cut from 0.5 mm thick sheet of the alloy. The high-purity oxygen-free copper bars (approximately 1 mm x 1 mm x 10 mm) were mechanically polished to a 0.05 µm colloidal silica finish, and masked with graphite, leaving a 1 mm x 1 mm area for the solder to bond. The unmasked region of each copper bar was coated with a thin layer of mildly activated rosin flux in order to optimize wetting. The copper bars and solder were then fixed in place using a jig to maintain the alignment of the joint, and reflowed on a hotplate. The joint was heated to a peak temperature of 275 °C

and held above the melting point of the Sn-3.9Ag-0.7Cu alloy for 100 s. The joint was then air-cooled on an Al block that cooled at a reproducible rate of 1.7 °C/s. More details of the reflow processes for these joints can be found elsewhere (Jiang, et al. 2011).

2.3 Image Acquisition:

X-ray microtomography images by taking a series of X-ray absorption images as at different angular orientations. The X-rays are generated in a cone-shaped beam from an x-ray tube. The sample being imaged is placed between the x-ray source and a 2D detector, and the transmitted X-rays are counted based on the location they impact the detector. The detector itself is composed of a thin scintillating material such as CsI which converts the incident X-rays to pulses of visible light and an optical CCD camera. The camera, typically containing 2048x2048 pixels and able to record 16 bits worth of data counts the pulses on the scintillator, producing a 2D projection image. The fraction of transmitted x-rays reaching a specific pixel is dependent on the linear mass absorption coefficient of the material between the source and that pixel. For a homogenous material, the transmitted intensity (I) is given by:

$$I = I_0 exp(-\mu x) \quad (1)$$

Where I_0 is the incident intensity, is the linear mass absorption coefficient, and x is the sample thickness. When the x-rays pass through different phases as in a real

material, the mass attenuation becomes the sum from all of the contributing phases:

$$I = I_0 \, exp(-\int \mu(x) \, dx), \quad (2)$$

To extend the mass attenuation information into 3 dimensions, projections are taken at different angles through the sample. Typically this is done by fixing the source and detector, and rotating the sample in the beam path. A typical image set consists of ~1000 projections taken over a 186° arc. These projection images are then reconstructed into a three-dimensional dataset using a Fourier transform-based reconstruction algorithm. The end result of the reconstruction process is a 3D dataset that can then be sliced into the parallel cross sections used in this study.

Imaging of the solder joints was done using a MicroCT-200 X-ray microtomography system (XRadia, Concord, CA,). Each acquisition consisted of 745 images, taken at angular increments of 0.25° . They were acquired at a specimen-source distance of 35 mm, a specimen-detector distance of 8 mm, and an accelerating voltage of 150 kV. These settings resulted in a resolution of approximately 2 μm. These images were reconstructed using Xradia's Reconstructor software into a 3D model of the microstructure which was subsequently sliced into a stack of parallel cross sections. The reconstructed images had a cubic voxel size of 2.16 um.

2.4 Segmentation Using 3D Livewire

The image datasets were segmented using commercial tomographic reconstruction software (Mimics 13.1, Materialise, Ann Arbor, MI). Segmentation was done by dividing the dataset into masks (corresponding to solder, pores, and the "background"). Simple thresholding was inadequate for separating solder and pores, due to relatively low contrast. This was especially true for smaller pores (< 20 μm). We used a Livewire algorithm, implemented in 3D in the Mimics software, to segment the pores. Working on a virtual cross section of the joint, the operator selects a starting point for segmentation along the edge of a feature of interest. The software then generates in real-time a livewire connecting the starting point with the current location of the cursor. (Figure 2a) The livewire line strongly tends to follow edges, and is guided by the user completely around the feature in a loop through the selection of additional points. The result is a quickly defined, accurate boundary contour that delineates the feature from the rest of the image.(b) To complete segmentation of the feature in 3D, a second contour is drawn on an orthogonal plane, at which point the software automatically contours the feature on the third orthogonal plane, creating a 3D mask of the object.(c). This mask is then used to create the 3D model (d).

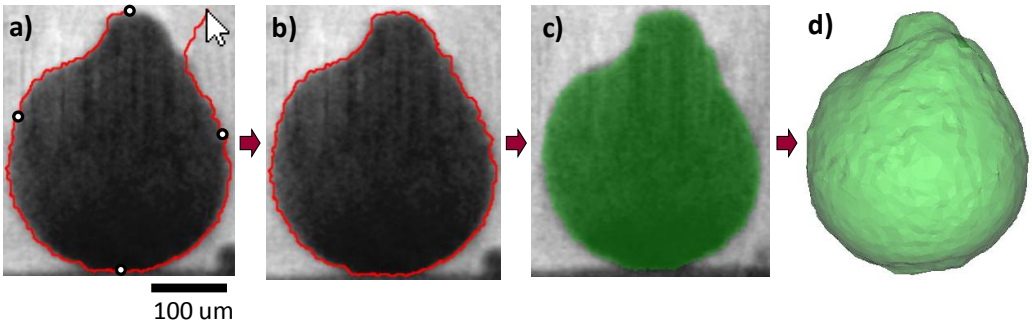

Figure 2: Segmentation using Livewire: Pores are first outlined with livewire contours though the user selection of seed points (a). The livewire calculates the optimal path between the previous seed point and the location of the cursor on the fly. Note that it closely follows the pore boundary. Completed contours (b) are then used to create a mask of the pore (c), which is then used to create a 3D model (d)

Simple high contrast geometries can be segmented with as little as one contour in each of the two manually defined directions while complicated shapes often require several contours. In this study, Livewires were drawn on approximately every 4th slice through the pore, making a typical 20um diameter pore require 5 contours drawn in each of the two manually defined directions and taking around 2 minutes to segment. A typical contour is drawn with 4 nodes spaced approximately equally around the pore. To aid in segmenting the pores in the case where they intersected the Cu, a plane was drawn across the Cu/solder interface. This produced a boundary to the Cu bar that was consistent for all pores, increasing the accuracy of the livewire contours in the situation where the Cu/pore interface could not be resolved.

The Livewire tool is able to follow edges by assigning a “cost” to every possible path between the starting point and cursor. Paths that have the characteristics of

an edge will be given lower costs through the use of a local cost function. The cost function in Mimics gives the cost of travel from a pixel p to an adjacent pixel q as:

$$l(q)= \omega_G \cdot f_G(q) + \omega_Z \cdot f_Z(q) \quad (3)$$

Where ω are weight terms that add to unity, f_G corresponds to gradient magnitude, f_Z to Laplacian zero-crossing. The gradient magnitude term assigns a low cost to pixels with a high 2D color gradient, a common feature of interfaces or edges in images. The Laplacian zero-crossing term uses local maxima in gradient to identify edge pixels, assigning them a low cost. The path calculation also considers an "attraction parameter" that determines whether small cavities in the boundary of an object are followed closely or bridged. Both the weight factor and the attraction parameter can be modified by the user. (Poon, Hamarneh and Abugharbieh 2008) (Mortensen and Barrett, Interactive Segmentation with Intelligent Scissors 1998) (Mortensen and Barrett, Interactive Live-Wire Boundary Extraction 1997) (Falcao, et al. 1998) (Guide n.d.) (Personal Correspondence with D. Beski 2012)

While the Livewire technique is more time consuming than the simpler thresholding segmentation technique, an accurate, repeatable representation of each of the pores in the joint is critical to correctly simulating the joint behavior in 4D, and Livewire's semi-automatic approach better captures the pore boundaries

than user defined threshold limits. After segmentation, the body of the solder and each of the included pores were reconstructed in 3D in Mimics. This was accomplished by applying a surface mesh to each mask, with a smoothing algorithm applied to remove surface artifacts from the reconstruction process. The smoothing parameters used were 2 iterations of smoothing with factor 1.0, 10 iterations of advanced edge triangle reduction with angle 60^{o}, and a 2x2 matrix reduction. These settings consistently produced smooth 3D models suitable for FE meshing, an example of which is shown in Figure 2(c).

2.5 Interrupted Experiment

To track the evolution of the Sn-alloy microstructure during shear deformation, the lap shear joint was first imaged in the as-reflowed state using the MicroCT-200 and then loaded in shear using a microforce testing system (Tytron 250, MTS Systems, Minneapolis, MN). The joint was sheared at a constant strain rate of 10^{-3} s^{-1}. After a set strain was applied, the sample was removed from the test fixture and imaged again. This process was repeated several times, producing tomographic datasets at 0, 0.05, 0.12, 0.18, and 0.44 shear strain. The interrupted shear stress-shear strain curves from each step are plotted in Figure 3, showing good agreement with the curve produced by uninterrupted shear loading of a comparable joint.

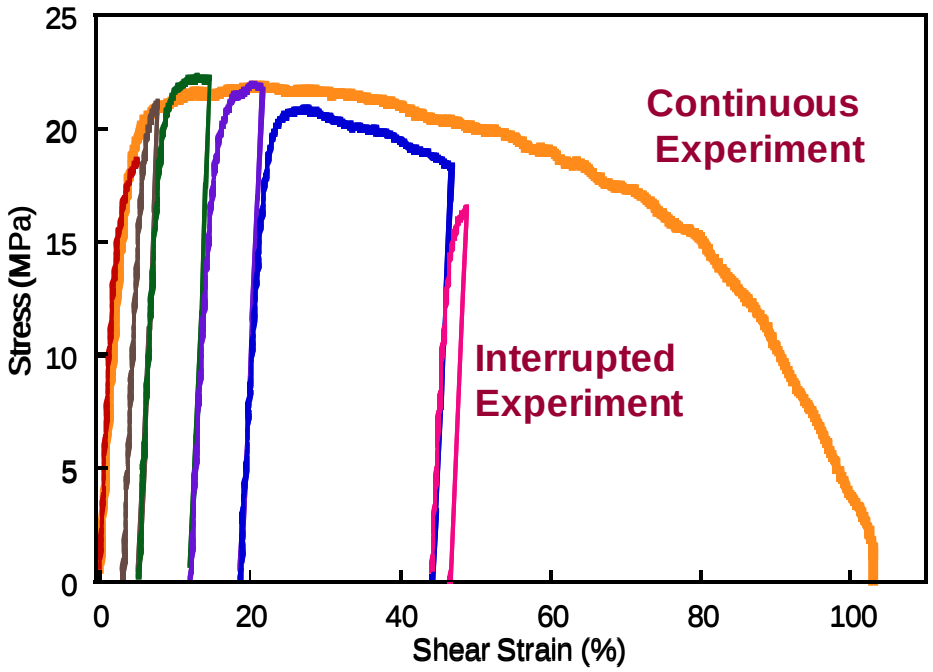

Figure 3: Experimental stress-strain curves measured during interrupted loading experiment. A curve produced by a monotonic (non-interrupted) loading test is provided for comparison.

The shear strain was measured using two different techniques. The first consisted of measuring the displacement using a displacement gage attached to the loading arm of the microforce testing system, and dividing by the thickness of the joint. The second method corresponded to measuring the displacement of the solder from the images obtained from x-ray tomography. Both measurements show good correlation at all of the strains measured.

2.6 Sphericity

To quantify shape change of a 3D object, several shape parameters have been used. In this study, since the pores are all compact and in general close to

spherical when formed and elliptical when deformed, the sphericity of the pores was used to measure their shape. The sphericity (Ψ) of a pore is given by the ratio of the surface area of a sphere (with volume equal to the pore volume) to that of the pore:

$$\Psi = \frac{A_s}{A_p} = \frac{\pi^{1/3}(6V_p)^{2/3}}{A_p} \quad (4)$$

Where A_s and A_p refer to the surface area of the sphere and pore respectively, and V_p is the pore volume. This surface area ratio can be reduced to a function of the pore's surface area and volume which are easily measured from its 3D reconstruction. Sphericity measures a shape's departure from perfectly spherical (Ψ=1), and since the joint in this experiment is loaded in a single direction, the pores should elongate plastically in that direction causing a decrease in sphericity with strain.

2.7 Sphericity Change due to Deformation

The deformed tomography images show that most of the strain was localized to the lower half of the joint. This localization is likely due to two factors. First, as seen in Figure 1, There exists a taper in the joint. Secondly, the two largest pores are both located on the lower interface. (Note, all references to "upper" or "lower" solder/Cu interface refer to the joint in the orientation seen in Figure 1. All references to the joint in this document use this orientation.) The combination of these two effects result in the cross sectional area of the solder

about 50 um (10% of the joint thickness) from the bottom interface being about 25% lower than 50 um from the top interface. This strain localization causes the sphericity of the pores in the localization band to decrease at higher rates than elsewhere.

By measuring the sphericity of the pores, the local state of deformation around each pore can be measured at a specific point in time. In this experiment, Sphericity analysis was applied to a set of 25 pores in the joint of a variety of sizes and locations. The sphericity of the pores was measured at 0.00, 0.12, 0.18, and 0.44 strain. The measured sphericity as a function of strain for these pores is shown in Figure 4. A 3D model showing the plotted pores is shown in Figure 5.

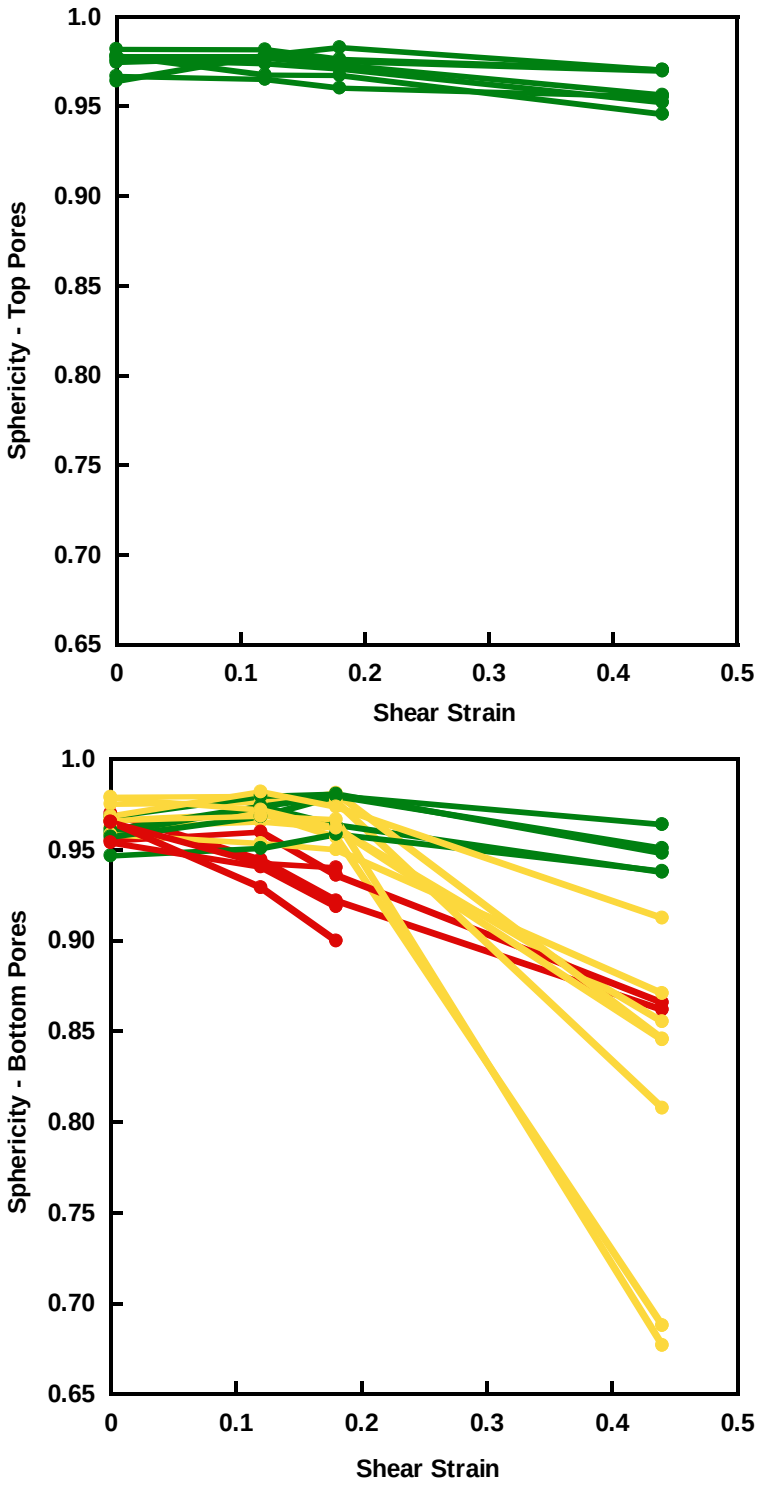

Figure 4: The sphericity decrease with strain is shown for pores on the top and bottom interfaces. The line colors correspond to early deformation (Red), late deformation (yellow) and no deformation (green).

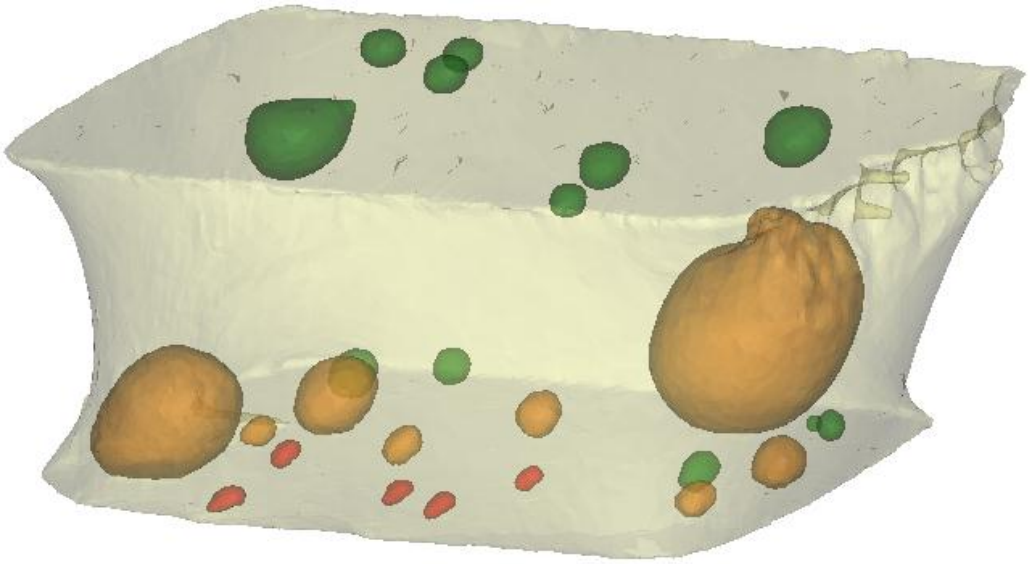

Figure 5: Solder joint model at 30% shear strain. The pores shown and coloration correspond with the plots in Figure 4.

The two plots show the behavior of pores on the top and bottom of the joint, and the first conclusion that can be drawn from the data is that the pores on the top interface do not show a significant sphericity change throughout the experiment. These pores were located well away from the crack path, and the fact that they don't deform agrees with other experiments (Yunus, et al. 2003). When looking at the pores on the bottom interface, a variety of sphericity change behaviors is observed, which can be broadly grouped into three types. The first type of pores are those that show deformation at low strains, before the crack was observed. These pores are noted in red in the plot, and are seen to occur in a cluster in Figure 5. This cluster is located near the front left corner of the joint, where the crack is predicted to initiate by FE simulation. The early onset of deformation in these pores agrees with this prediction, and it is through these pores that the crack is observed to propagate at high strain. For this reason the

sphericity of some of the red pores cannot be measured above 0.18 strain due to coalescence during cracking.

A second group of pores shown in orange shows very little sphericity change up to 0.18 strain, but have a significant drop after that point. In 3D it is seen that these pores are farther away from the crack initiation site than the red pores, which indicates that these pores experienced significant plasticity only after the crack had begun to propagate. Note that the large pore in the front left corner shows this type of behavior. Looking at Figure 1, it is clear that the deformation in this pore is localized to a narrow band near the cu interface, while the upper two-thirds of the pore shows little deformation throughout the fracture process. Since sphericity measures the deformation of the pore as a whole, the small deformation near the interface didn't produce a measureable change in sphericity at low strain.

The third group of pores, shown in green are those that didn't exhibit a significant sphericity change throughout deformation. As mentioned previously, all of the pores at the top of the joint exhibit this behavior, as well as pores on the bottom that are far away from the crack propagation path (rear left corner). In the rear right corner of the joint, the crack is observed to deflect upward though the large pore, which shields the pores between the large pore and specimen edge from deformation, giving them this sphericity behavior.

The ability to characterize local deformation within the joint is important for the validation of deformation and failure simulations. The sphericity behavior

quantified here should be replicated by a robust damage prediction model, and indeed this comparison is made in Chapter 4.

2.8 Conclusion:

X-ray microtomography was used to image a Cu/Solder/Cu joint in 3D at a variety of strains. The damage in the joint was quantified by measuring the sphericity change of the reflow porosity as a function of strain. The pores in the joint were shown to exhibit three types of sphericity behavior, and each of the behaviors were correlated to the position of the pores in the joint. The sphericity of pores near the crack initiation site drops measurably before the crack initiation is observed, and it is through these pores that the crack is observed to propagate at high strain.

Chapter 3

QUANTIFYING THE ERROR IN ACQUISITION AND 3D MODELLING

3.1 Introduction:

Tracking the sphericity change is a useful tool for quantifying the deformation in the sample. An important question to address when quantifying data is the error involved in the process. Since these models were intended for FEM modeling, there is a volume change associated with A) Segmenting the raw images into masks representing solder and pores, B) Taking the masks which are composed of all of the voxels assigned to a given phase and constructing a 3D model (surface mesh), C) Converting the surface meshed 3D model into a volumetric Finite element mesh.

3.2 Segmentation Error:

To quantify the segmentation error, a solder joint was polished such that pores were present on the polished surface. The sample surface was then imaged with an optical microscope, and the whole sample with x-ray tomography. The comparison was made by first determining the scaling factor between the two datasets. Then, the data was segmented using Livewire as above, and the size of the pores at the surface was measured on the mask and optical images.

It should be noted that the error in this analysis is typically a fixed number of voxels rather than a constant percent error. Thus, it is more useful to measure the error in terms of radius than as a volume percent. (±1 voxel error in pore radius is 27% volume difference for a 20 um diameter pore, but 4% for a 150 um

diameter pore). Thus the error in pore size was calculated by converting the area of the surface feature masks and the volumes of the 3D model and volumetric mesh into an equivalent size term. This term is defined for surface measurements as

$$r_s^* = \sqrt{\frac{A}{\pi}} \tag{5}$$

Where r_s^* is the equivalent size and A is the area, and for volume measurements as

$$r_V^* = \sqrt[3]{\frac{3V}{4\pi}} \tag{6}$$

Where r_V^* is the equivalent size and V is the volume. The equivalent size is equal to radius in the case of a circle (2D) or sphere (3D). To calculate the uncertainty associated with each of the three steps, the change in equivalent size was measured for a number of features, and the standard deviation (σ) of the result calculated. Twice the standard deviation (2σ) gives the 95% confidence interval for the expected volume change associated with that step.

A comparison of a surface feature as seen by optical microscopy and microtomography is shown in Figure 6. The difference in equivalent size measured with these two images is 0.63 voxels which is typical for these measurements. While the error in the equivalent size of a surface feature is not the same as that for a 3D feature, they are similar. Based on this analysis, the

expected uncertainty in size between the actual feature and its segmented mask is σ=0.58 voxels.

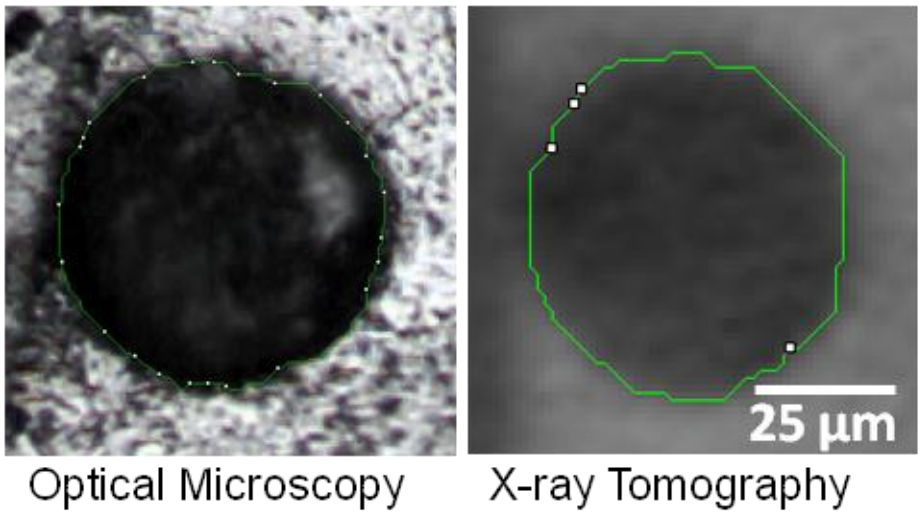

Figure 6: Comparison of a pore intersecting a polished surface as seen by optical microscopy and tomography.

3.3 3D Modeling Error

Once the masks were created, they were used to construct 3D models of the pores. In order to produce 3D models that could easily be turned into volumetric FE meshes, smoothing was applied to reduce the surface roughness of the model and eliminate surface artifacts. A side effect of any smoothing operation however is that the volume of the cubic voxels isn't exactly maintained in the smoothed model. To measure this, the volume change from mask to 3D was calculated for each of the 25 pores used in the sphericity analysis. The equivalent size change is then plotted as a function of pore size in Figure 7. For the pores in this sample, the measured radius change from the 3D modeling step had a standard deviation of 0.47 voxels.

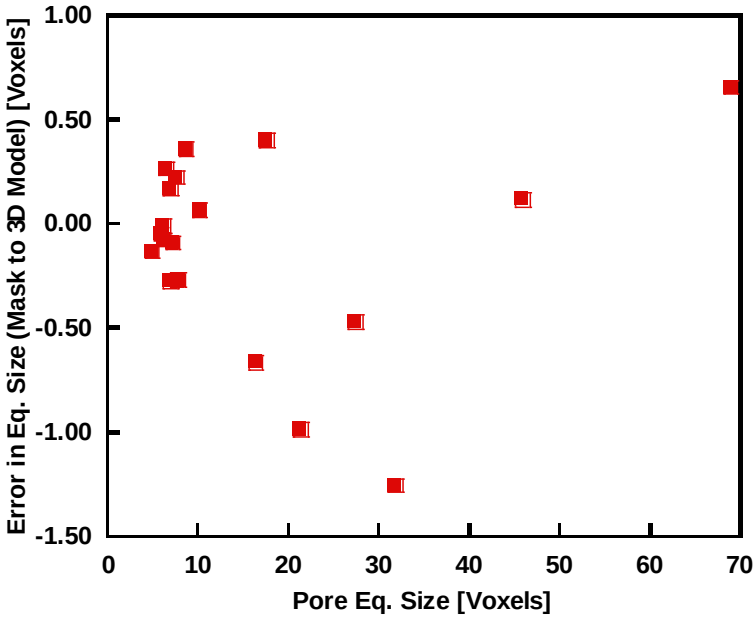

Figure 7: Measured change in equivalent size upon conversion from mask to 3D model

3.4 Volumetric Meshing Error

The last contribution to error applies if the 3D model is made into a volumetric mesh. Typically, the surface mesh produced by Mimics contains a large number of high aspect ratio triangles. These must be changed into low-aspect ratio elements for accurate modeling. Using the meshing techniques described in (Padilla, et al. In Press), the equivalent radius change for the pores is shown in Figure 7. With the techniques and parameters described here, this is the smallest contribution to the total error in this process with a value of σ=0.17 voxels. It is possible that the total error would be lower if less smoothing was applied when creating the 3D models and more during the volumetric meshing, but this has not been explored.

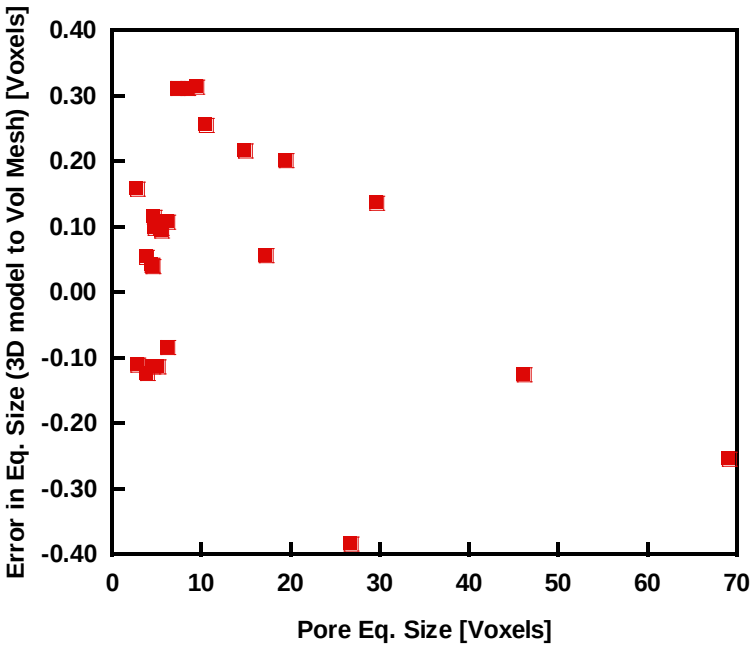

Figure 8: Measured change in equivalent size from 3D model (surface mesh) to volumetric mesh for finite element model.

3.5 Variability in Segmentation Due to User

While the above analysis shows the volume difference between the actual feature and the segmented mask, the user-guided nature of Livewire means that a small variation in size and shape is expected if a feature is segmented multiple times. To determine the effect of this variability on the measured sphericity, a 30 um (slightly larger than median pore size) pore was segmented multiple times by the same operator. The operator is experienced in this type of segmentation, and used the technique outline above on each attempt. The volume and surface areas of the 3D models produced in the ten attempts are shown in Figure 9 (top). It is clear from inspection that there is a strong correlation between the volume and area changes between attempts. Since sphericity is a ratio of these two measurements, it is expected that the variation in sphericity to be lower. The

sphericity measured on each attempt is shown in Figure 9 (bottom). The average and standard deviation of these plots is shown in Table 1. When the relative standard deviation of the three parameters is calculated, it is seen that the standard deviation of the sphericity is less than 1% of its measured value, indicating that the variability of livewire, if done in a consistent manner makes an insignificant contribution to the error in measured sphericity. This means that when comparing different datasets taken with the same acquisition and processing parameters, the human error will be negligible.

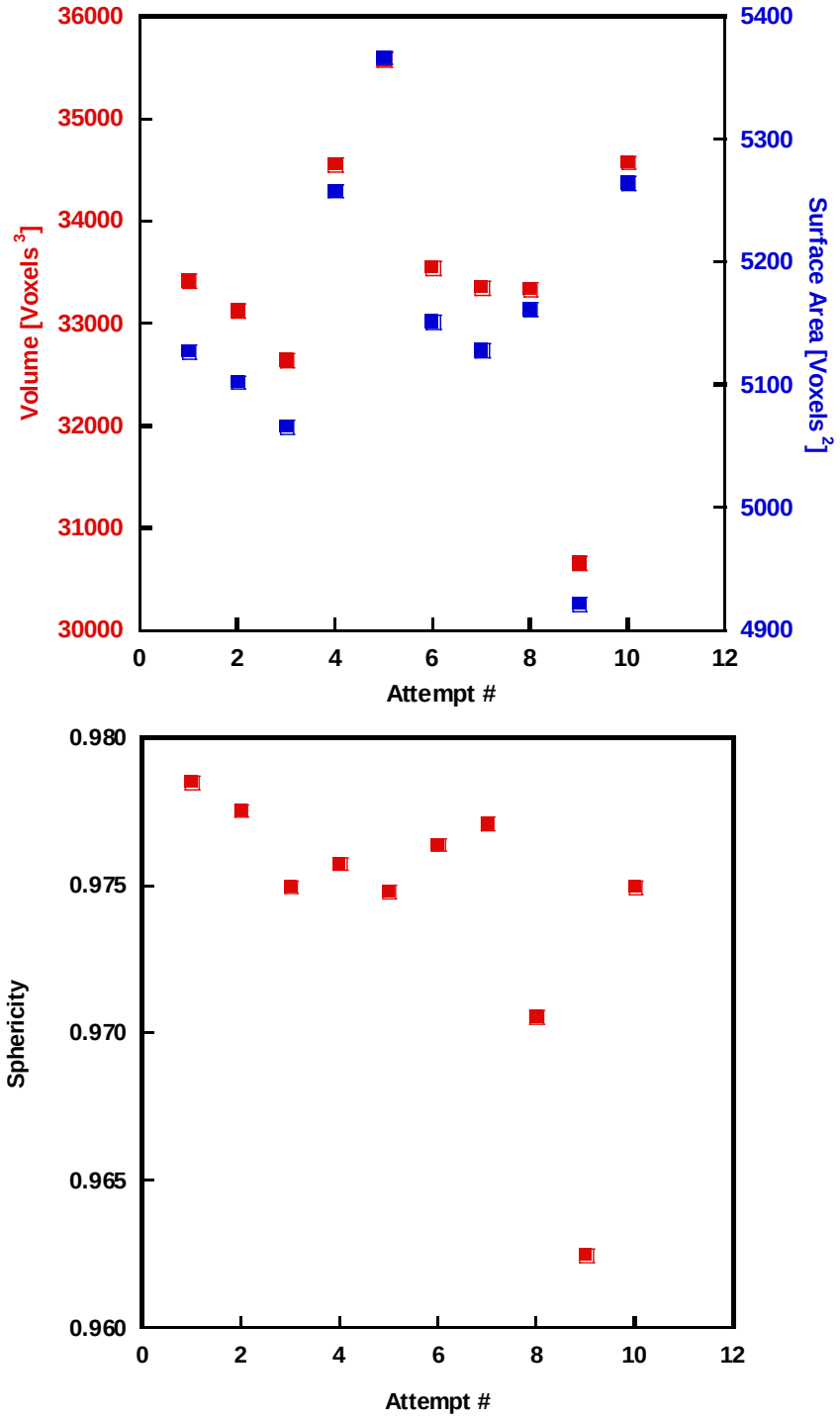

Figure 9: Top: Measured surface area and volume from repeated segmentations of the same pore. Note the strong correlation between the two measurements. Bottom: Measured sphericity for each of the attempts.

	Volume	Surface Area	Sphericity
Mean (μ)	33480	5155	0.9743
Standard Deviation (σ)	1317	122	0.0047
Relative Standard Deviation (σ/μ) a.k.a. Coefficeint of Variation	0.039	0.024	0.005

Table 1: Statistics on the size and shape measurements from 10 Livewire-created 3D models of the same pore.

This result also suggests that when measuring sphericity, the error due to the different processing steps is likely to be smaller than the measured error in size. This is because the volume change during all three processing steps tends to dilate or contract the pore boundaries while maintaining their shape.

3.6 Propagation of Error and Conclusions:

The error in the process of acquiring, segmenting, creating 3D models, and volumetric meshing the tomography data was measured. The results indicate a strong size dependence on experimental error, with the error due to acquisition and segmentation having σ=0.58 voxels, the error to 3D modeling having σ=0.47 voxels, and the error in volumetric meshing σ=0.18 voxels. To calculate the total uncertainty for the entire process, the individual components can be added using the formula:

$$\sigma_{total} = \sqrt{\sigma_A^2 + \sigma_B^2 + \sigma_C^2} \quad (7)$$

Where σ is the standard deviation, and A, B and C refer to the three individual contributions. In this case σ_A=0.58, σ_B=0.47, σ_C=0.18. Thus, the combined uncertainty comes to σ_{total}=0.77 voxels. This means that 95% of pores will

undergo an equivalent size change of less than 1.54 voxels during the imaging and segmentation, and meshing process.

Chapter 4

VALIDATION OF MICROSTRUCTURALLY REALISTIC FINITE ELEMENT MODELLING.

4.1 Introduction

Several studies have been conducted using Finite Element modeling to predict the effect of porosity on failure. Terasaki and Tanie (Tanie and Terasaki 2005) conducted three-dimensional FE modeling of solder joints with spherical and hemispherical voids. They concluded the distance between a void and the surface had a significant impact on crack growth. Gao et al. (Gao, Yi, et al., The Effect of porosity on the fatigue life of cast aluminum-silicon alloys 2004) and Xu et al. (Xu, Wen and Zhai 2011) showed similar results based on pore size and location in Al alloys, and Gao et al. (Gao, Yi, et al., A micro-cell model of the effect of microstructure and on fatugue resistance in cast Al alloys 2004) also showed that spherical porosity caused enough stress intensification around the pore to debond nearby Si-particles from the matrix and significantly reduce the fatigue limit. Li et al. (Li, et al. 2006) and Shen et al. (Shen and Brinson 2007) modeled the effect of pores on the strength of Ti. Unfortunately, most of the modeling studies described above incorporate an over-simplified geometry of the microstructure. Hence, the results obtained from these analyses cannot be experimentally verified.

A clear understanding of the influence of pore size, shape and distribution in the solder joint is required to understand the effect of the microstructure on plastic deformation behavior of these materials. The onset of strain localization due to porosity is a complex function of pore size, pore clustering, pore spacing, and pore shape. Generally, it is known that larger pores have more influence on mechanical behavior but the effect of smaller pores cannot be neglected, particularly when there is clustering of the pores. Furthermore, pores that are very closely spaced will be highly susceptible to strain localization (Chawla and Deng, Microstructure and mechanical behavior of porous sintered steels 2005) (Chawla, Williams, et al. 2009). Thus, it is important to have a thorough knowledge of the influence of pore characteristics and, the interplay between them, on the deformation behavior of metallic alloys. For this purpose, a microstructurally realistic Finite Element model of the solder joint was created to simulate plasticity and failure.

Our previous work (Chawla, Sidhu and Ganesh, Three-dimensional Visualization and microstructure-based modeling of deformation in particle-reinforced composites 2006) has shown that numerical models incorporating only a simplified geometry of the microstructural features do not accurately reproduce the macroscopic stresses and strains. Indeed, the stress and strain state can only be represented accurately using models that incorporate the true geometry of the microstructural features. Fortunately, the X-ray tomography data obtained in the interrupted experiment is suitable for this purpose. The approach used in this experiment is shown schematically in Figure 10. Interrupted lap shear tests,

combined with X-ray tomography, were conducted at different strain levels to visualize the damage evolution within the joint. It will be shown that the FEM predictions are in good agreement with the X-ray tomographic observations. Thus, the combined approach of tomography and numerical modeling can be used as an effective means of predicting failure of the solder joint.

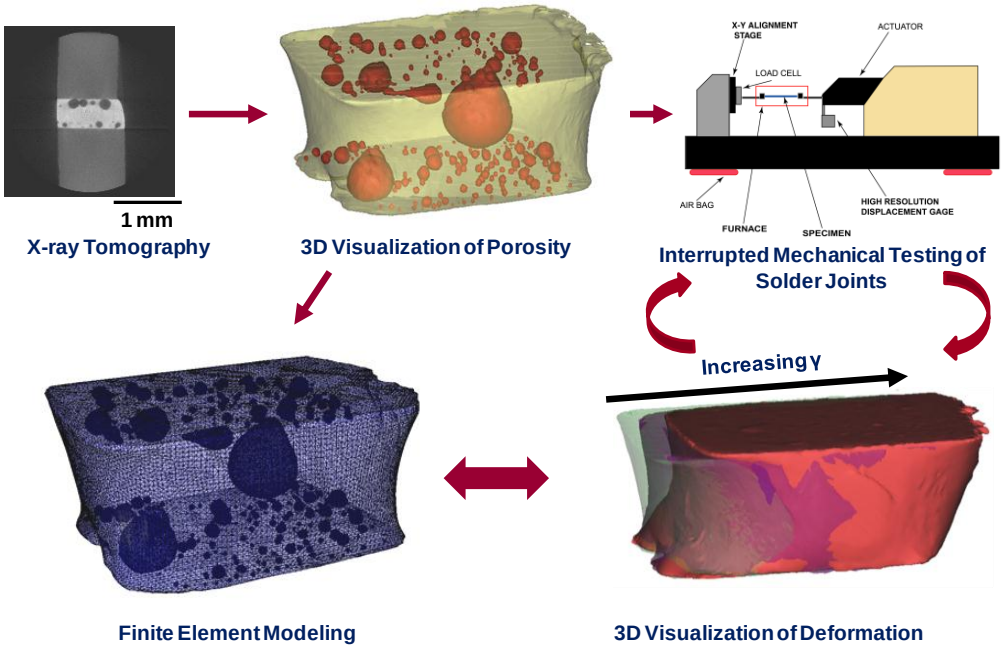

Figure 10: Schematic of experimental and simulation approach, based on 3D microstructures, for quantifying damage in Sn-based solder alloys.

Representative 2D images of the joint at different stages are shown in Figure 11(a). After acquisition, the joints were segmented using the livewire algorithm and reconstructed in 3D (b). Note that due to the time required for segmentation and the difficulty in segmenting cracked/coalesced pores, only a fraction of the pores are shown in the deformed models in (b). The deformed tomography images show that most of the strain was localized to the lower half of

the joint. At intermediate strain (γ=0.18), no cracking is observed but the pores on the lower half of the joint elongate while the pores in the upper half remain relatively unchanged. After the onset of fracture (γ=0.44), cracks are seen propagating through the pores near the lower solder/Cu interface, and the few pores that are not split by a crack show very large elongation. Using x-ray tomography to image the joint at intermediate stages of strain allows the progression of deformation to be compared to the FEM model (c). These results are presented in the next section.

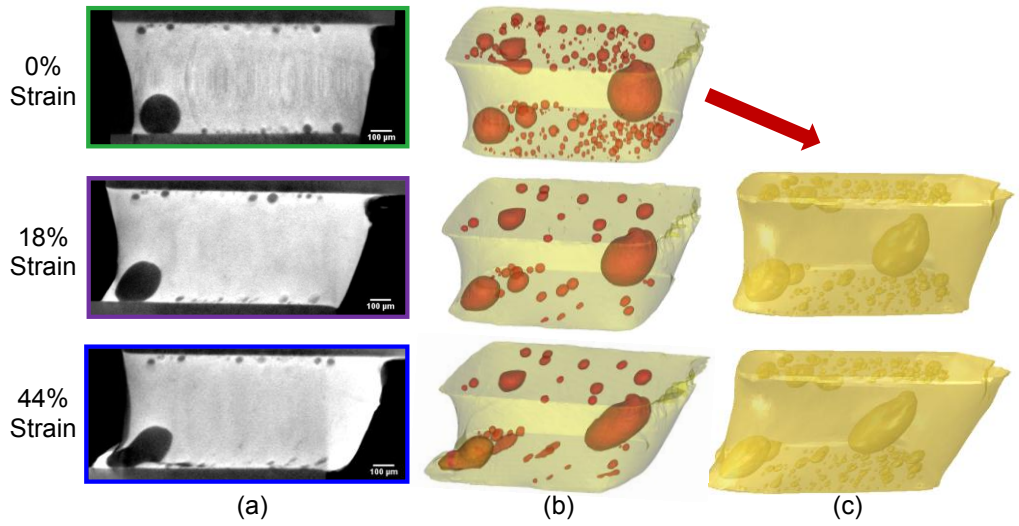

Figure 11: (a): Cross sections of a similar plane though the solder joint at indicated shear strains. (b): 3D reconstructions of tomography data showing solder (yellow) and reflow pores (red). At 18% and 44% strain, only those pores with significant deformation are shown to assist in visualization of shape changes of the pores. (c): Deformed FEM models produced by simulating shear deformation of 0% reconstruction, showing good agreement with experiment.

4.2 Microstructure-based Finite Element Modeling

Finite Element Modeling (FEM) was used to model the deformation of the solder joint and to predict the initiation and propagation of cracks by

incorporating a progressive ductile damage model (Shen, et al. 2005) (Lee, Lee and Jung 1998). The reconstructed 3D model of the unstrained joint was imported into commercial meshing software (Hypermesh, Version 9.0, Altair Engineering Inc., Troy, MI) to generate a volumetric mesh. The meshing was conducted using linear tetrahedral elements (C3D4) in such a way that there was a highly refined mesh around the region of all the pores as shown in Figure 12(a). The mesh was made more coarse in the matrix so that the total number of elements in the final model did not significantly increase computation time. The final meshed model has 1,728,106 elements. The meshed model was exported to Abaqus (Version 6.10, Dassault Systems Simulia Corp, Providence, RI) for the failure analysis.

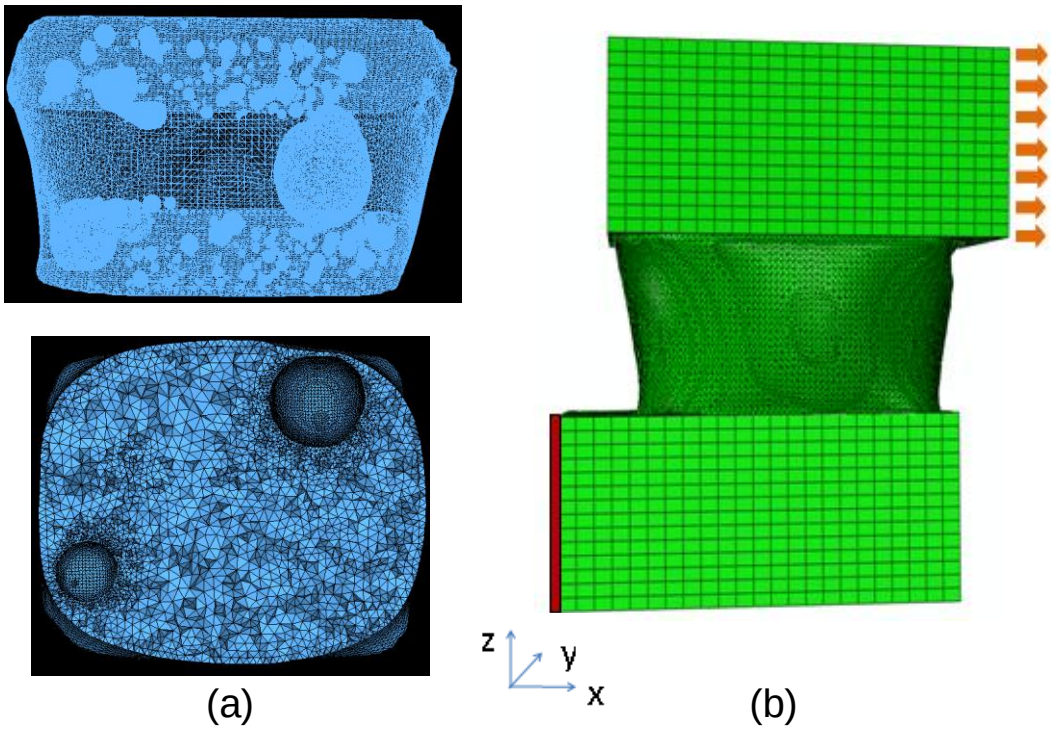

Figure 12: (a) Meshed model showing the pores. A cross section along the thickness of the joint shows the refined mesh around the pores and a relatively

coarser mesh in the matrix. (b) 3D model for FE analysis. The copper bar on the bottom was fixed in all the three translational directions and the copper bar on the top was fixed in y and z direction and displaced in x direction. (Courtesy of V. Jakkali)

The 3D computational model used for the analysis is shown in Figure 12(b). The solder joint is attached to copper bars at the top and bottom of the joint as in the physical joint. The copper bar at the bottom is fixed in all the three translational directions. The copper bar at the top is fixed in y and z directions and a displacement is applied in the x direction to deform the joint in shear. More specifics of the Finite Element model can be found in (Padilla, et al. In Press)

The progressive ductile damage model available in Abaqus was used to simulate the plastic deformation and ductile failure of the solder joint. A schematic of the ductile damage response of a material is represented in terms of the stress-strain curve shown in Figure 13.

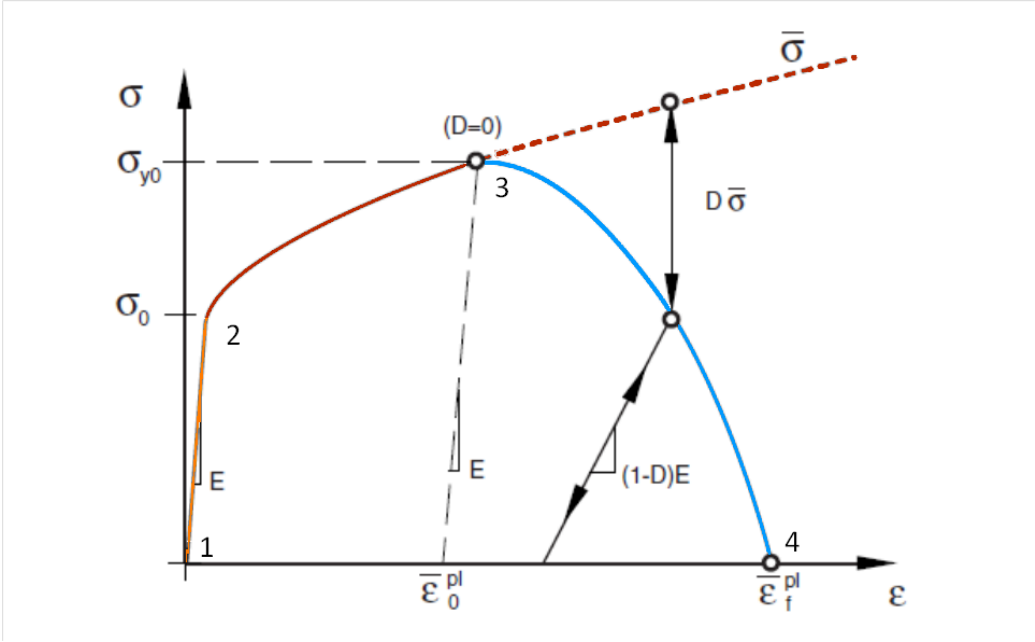

Figure 13: Schematic Representation of the Ductile Damage Model (Dassault Systems Simulia Corp 2010).

At low strains, the solder material is modeled with elastic plastic behavior. The material is assumed to be linear elastic between the points labeled 1-2, and deform plastically between points 2-3. The plastic part of the curve (2-3) is based on experimental stress-strain data of bulk solder. Beyond point 3, there is a reduction in stress carrying capacity of the material with increasing strain until failure occurs at point 4. This material response is implemented in each element in the mesh. Thus, an element reaches the material failure point, it is removed and a crack is developed in the model. As the deformation increases, more elements reach the failure criterion and the crack grows through the model.

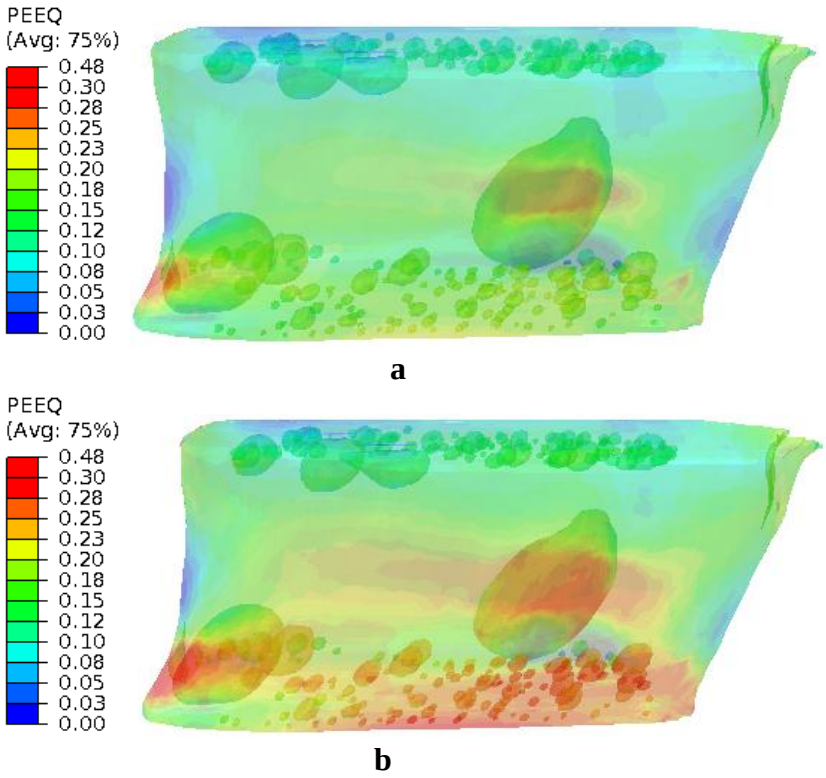

Figure 14: Plastic Equivalent strain plots at a) ε = 0.37 b) ε = 0.4. Higher strain localization is seen at the bottom interface around the vicinity of the two large pores (Courtesy of V. Jakkali)

Figure 14 (a) illustrates the plastic equivalent strain developed in the model at a nominal shear strain of 0.37. The two large pores near the bottom interface of the joint act as strain localization sites where the highest strain in the model is observed. As the model is deformed, the plastic equivalent strain (PEEQ) around each of the two large pores increases significantly as shown in Figure 14(b). Also, the bottom interface has higher strain than the top interface. This can be attributed primarily to the taper in the joint discussed previously.

Figure 11 (b,c) shows the deformation of pores observed experimentally and as predicted by the FE model. The FE results show very good correlation with the experiment. In both cases, more pronounced deformation is seen in pores on the lower half of the sample, located near the solder/copper interface.

The numerical model developed should not only predict the deformation of the pores correctly but also represent the failure of the joint accurately. Figure 15 shows a comparison of crack propagation path predicted by FE model and observed experimentally. Two 2D cross sections across the thickness of the joint depicting the crack in the sample are shown in the figure. The first cross section shown on the left in Figure 15 shows a crack around the pore located near the bottom left corner of the joint as observed in the simulation results and tomographic images. The crack is seen to nucleate around the large pore and propagates towards the interface in both the cases. The second cross section on the right shows the crack around the other large pore located at the bottom right corner of the joint. The FE model predicts crack nucleation in the same location where failure of the pore wall is observed experimentally. Comparison of FE results with experiment clearly demonstrated the capability of the numerical damage model to accurately simulate the deformation as well as the failure of the solder joint.

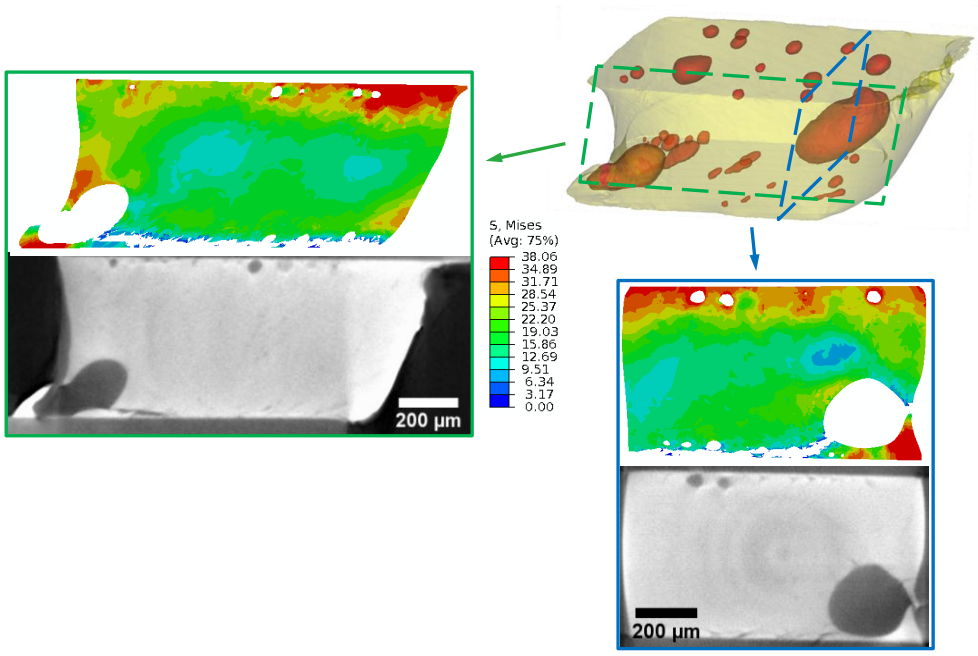

Figure 15: 2D sections across the thickness of the joint showing a comparison of crack propagation observed experimentally and that predicted by FE analysis. The crack propagation path predicted by the FE model correlates well with the actual crack propagation path.

4.3 Sphericity Comparison to FE and Simple Shear Models

In addition to correctly predicting the crack nucleation sites in the joint, the predictive damage model should correctly capture the strain localization that occurs around the reflow pores. The ability of a model to correctly predict strain localization can be measured by comparing the predicted pore shape change to experimental observation.

To measure the accuracy of the ductile damage model in predicting deformation of individual pores, the sphericity change for selected pores in the joint was simulated at several strain values by exporting the displacement values

of nodes on the surface of the pore from the Finite Element Model and reconstructing the pore in 3D using the same parameters as the experimental data.

To give a basis of comparison for the FE model's ability to predict deformation, a simplified model was also constructed to look at deformation of a single pore. A basic characterization of the deformation in the lap joint would be to assume that the body of the solder deforms homogenously in simple shear. This result would ignore any strain localization in the joint, and emphasize the necessity of its incorporation. To simulate simple shear deformation the segmented 3D masks of as-reflowed pores were exported to MATLAB where a shear transformation was applied in the loading direction. The transform for simple shear of a strain γ of a point (x,y) to (x',y') is given by:

$$x' = x + \gamma y \tag{8}$$

$$y' = y \tag{9}$$

A cross section of the pore mask before and after a 34% shear transformation is shown in Figure 16. Also shown is the 3D reconstruction of the pore at each value.

The sheared masks were then imported into the Mimics software and reconstructed as with the same parameters as the FE and experimental masks.

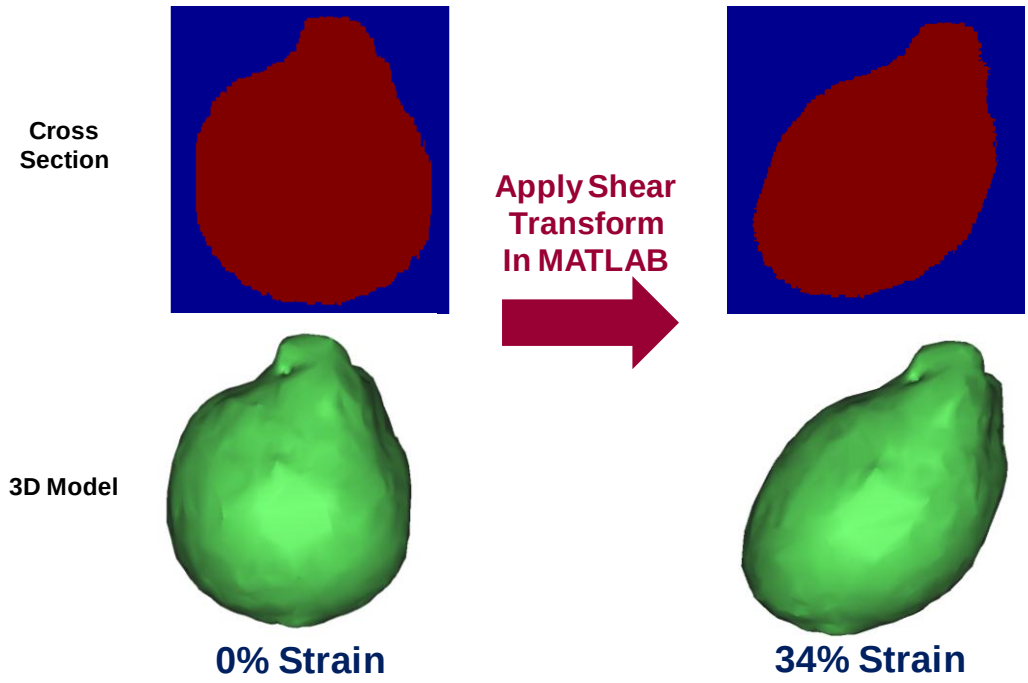

Figure 16: Top: 2D cross sections of the pore mask before and after simple shear transform. Bottom: The corresponding 3D models.

Once the pores were reconstructed from the experimental imaging and the FEM and simple shear simulations, a surface wrap algorithm was applied to each reconstruction to remove any artifacts. The sphericity of each reconstruction was then calculated from its volume and surface area. The sphericity measurements of representative pores on each of the top and bottom interfaces are plotted as a function of strain in Figure 17.

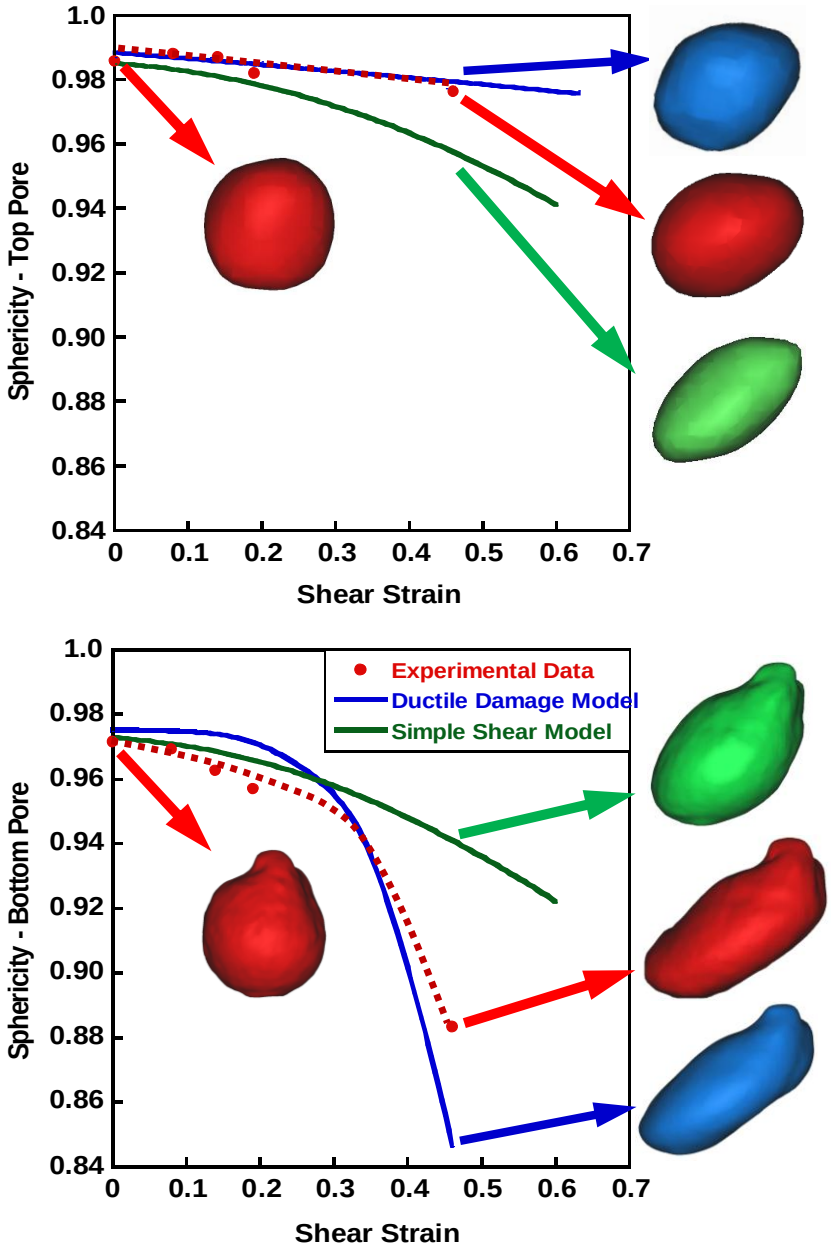

Figure 17: Sphericity measurements and corresponding 3D reconstructions of representative pores from the top and bottom interfaces. Each plot shows the sphericity change measured from 3D models of the experimental data (red) and the FEM and simple shear simulations (blue and green respectively). The bottom pore shows a steep sphericity drop while the top pore does not. This is consistent with the strain localization observed in the joint. In both cases the FEM ductile damage model is able to correctly capture the deformation, unlike the simple shear model. Deformed pore reconstructions are at 44% strain.

For the bottom pore at low strain values, all three curves show a gradual decrease in sphericity, with a drop-off occurring in the experimental and FE data around a strain of 0.35. This drop-off coincides with a higher degree of strain localization occurring in the joint at high strain. Accordingly, the simple shear deformation model does not predict this acceleration in deformation. In the top pore plot, the sphericity is seen to decrease very little as the joint is deformed. Again, the FE ductile damage model was able to simulate the experimental behavior much more accurately than the simple shear model showing that the ductile damage model does well at capturing both the true local deformation of the joint and its macroscopic failure.

Chapter 5

DIGITAL IMAGE CORRELATION MEASUREMENTS OF LOCALIZED STRAIN

5.1 Introduction:

The sphericity change measurements provided by the above analysis give a good measure of the local deformation occurring around the pores within the solder joint. An improvement on these measurements would be to measure the strain at every point in the joint, giving information that is directly comparable to the plastic strain map output by the finite element model. A 2D imaged based technique called Digital Image Correlation (DIC) has been used for some time to experimentally measure strains over the entire surface of a sample without the use of traditional strain gauges. The technique works by tracking the location of features on the surface as they move due to deformation. If a sample is imaged before deformation (Image A) and again after deformation (Image B), the software will identify a feature at coordinates (x,y) in A, and find its new location (x',y') in B. By tracking the relative displacement of many different marker features, it can then determine the strain field between them, and calculate the principle strains in the sample. As described, this process measures the surface strains in the sample. In recent years, this process has also been extended to 3D, with the name Digital Volume Correlation (DVC). Since X-ray tomography data is able to achieve the resolutions necessary to track reasonably small marker particles, several authors have applied DVC to tomography data.

An important consideration when designing a specimen for DVC is the choice for a marker material. In an ideal case, the microstructural features present in a material such as pores and secondary phases can be used for DVC analysis. I will term these intrinsic marker particles, as they would otherwise naturally occur in the material. Unfortunately for some materials, and SAC solders fall into this group, the secondary phases such as the Ag_3Sn and Cu_6Sn_5 intermetallics do not have significant enough differences in mass absorption coefficient from the matrix phase to be easily resolved, especially with lab scale tomography. Instead, artificially introduced or extrinsic markers are often used for this type of analysis. Chiang et al. (Chiang, et al. 2010) were able to track the displacement of glass beads blended into a dental composite to measure shrinkage during curing. Toda et. al (Toda, et al. 2011) used Pb particles in Al, and Haldrup, Nielsen and colleagues (Haldrup, et al. 2005) (Nielsen, et al. 2003) used W particles in powder metallurgy formed Al. Kobayashi et al. (Kobayashi, et al. 2008) and Nakazawa (Nakazawa, et al. 2008) used laser drilled holes as markers in a copper alloy. While using extrinsic markers allow the selection of high-contrast and often rigid materials, they inevitably effect the deformation behavior of the material being studied. To understand the natural behavior of a material, it should be imaged without extrinsic markers. In this chapter, eutectic PbSn solder is proposed as a solder alloy with high enough intrinsic contrast between phases to be suitable for Digital Volume Correlation. First, the 2D DIC process is demonstrated on a deformed solder surface using the solder phases as markers. Then 3D data is

presented that suggests that the material is a suitable candidate for the 3D technique.

5.2 Sample Preparation:

In this study, PbSn solder was chosen for its relatively high-contrast between phases and its simple Binary-eutectic microstructure. Alloys of Pb85-Sn, Pb60-Sn, and the eutectic Pb37-Sn composition were proposed as candidates for DVC. Due to the high absorption of Pb however, the Pb37 was chosen for in depth study after difficulty in CT imaging the higher-Pb content alloys. An ideal DVC alloy would contain homogenously distributed markers, so a quenched and then aged PbSn sample was used. The as-received PbSn microstructure contained very fine precipitates, and therefore was aged to coarsen the phases.

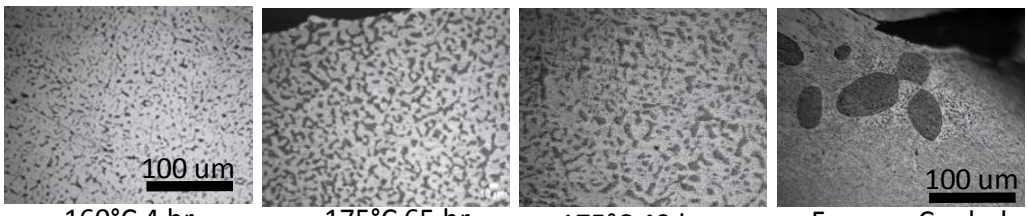

Figure 18: Optical Images of aged Pb37Sn Solder after heat treatment.

The microstructure taken after several aging treatments is shown in Figure 18. The coarsest microstructure was aged at 175°C for 40 hr and then 183°C for 88 hr. This sample contains proeutectic Sn phase particles around 10-30 μm thick. This sample was selected for future study, as each phase should be 5-15 pixels wide in the CT data. Slow solidification was also considered as an option to obtain a coarse structure, but the secondary phases particles nucleated only near

the sample periphery. The samples used in this study were 300 to 800 µm cubes hand cut from the aged eutectic alloy and mounted on 1 mm x 1 mm x 10 mm Cu bars using adhesive. These were polished to a 0.05 µm colloidal finish and imaged with optical microscopy in the 2D experiment and the XCT-200 tomography tool in the 3D experiment.

5.3 2D Digital Image Correlation

In order to test the suitability of the PbSn microstructure for 2D DIC, a solder sample aged at 175°C 60 hr was polished on one face and imaged using an optical microscope. The a series of ~10 images were taken of the surface at 500x and stitched together using the stitching tools in the Fiji software. The sample was then indented on the edge of the polished face using a Vickers micro-indenter, shown in Figure 19.

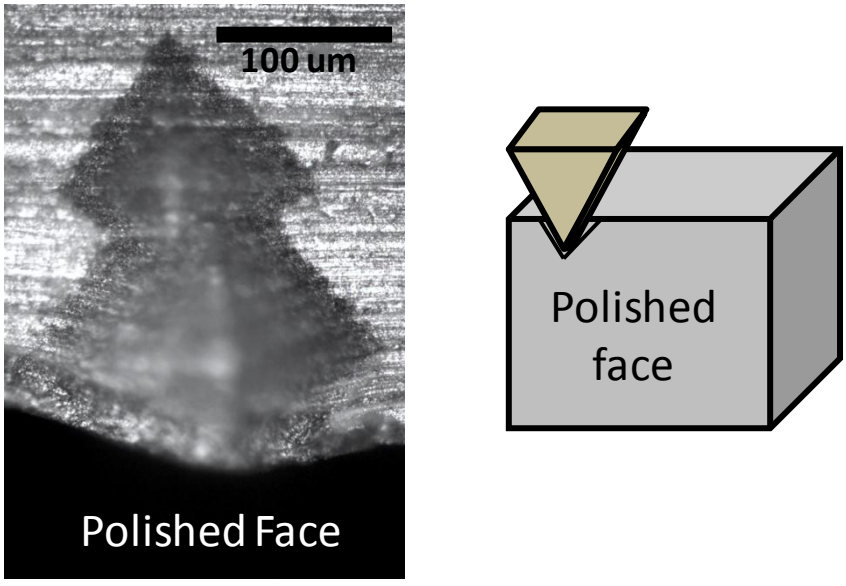

Figure 19: (a) Top view of Vickers indentation at sample edge. (b) Schematic of indentation location

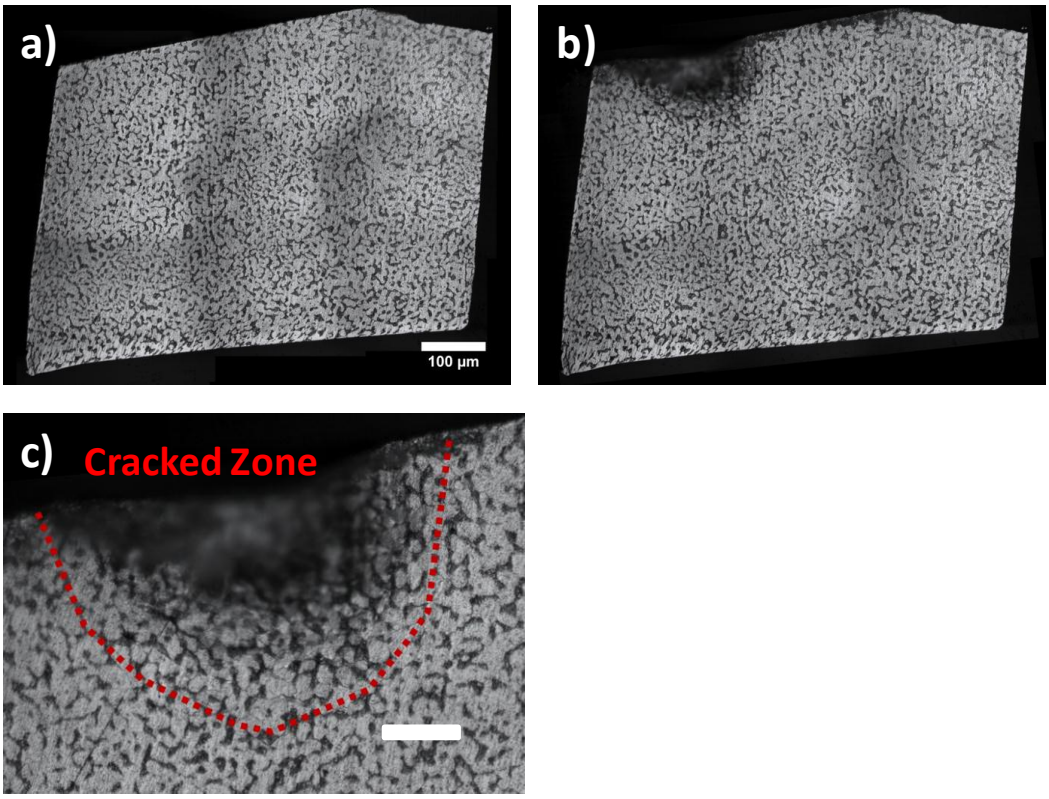

Figure 20: Optical images showing polished surface of sample before (a) and after indentation (b,c). (c) shows the extent of microcracking around the indentation zone.

This indentation introduced a significant amount of deformation as seen in the before and after images in Figure 20. Note that in the region around the indentation, there is a significant amount of micro-cracking at the surface. The extent of this damaged region is outlined in Figure 20. There are also some dark regions in the images; these are artifacts from the stitching process.

To perform the DIC analysis, the surface images were first registered using the non-deformed material far away from the indentation. Then the images were imported into the Aramis V.6.2.0 software. The software then tracked the displacement of the phases in the images, and produced strain contour maps of the

surface. Figure 21 shows the measured Von Mises equivalent strain for the region around the indentation.

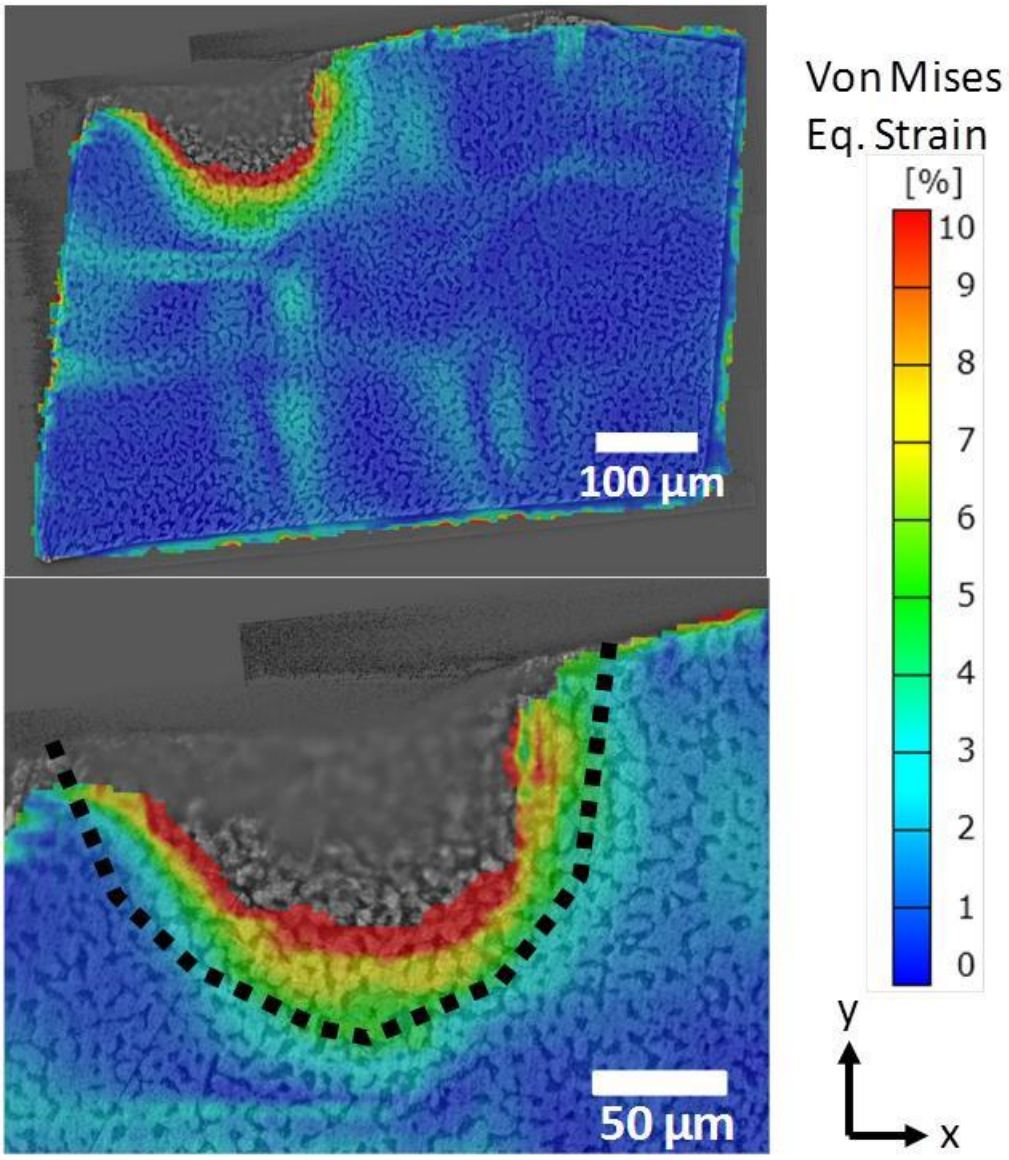

Figure 21: Equivalent Von Mises Strain measured using 2D DIC. Black dotted line on lower image corresponds to edge of cracked region.

The strained zone, shown in green to red extends about the same distance as the observed micro-cracks suggesting that the cracking occurs throughout the plastic deformation zone, at least at the sample surface. The fact that the 2D data gives a reasonable strain measurement suggests that the PbSn phases have the correct morphology for 3D DVC. More importantly, this measurement can be directly compared with the output of an appropriate finite element model.

5.4 Future Work: Digital Volume Correlation Data from 3D X-ray Microtomography

A PbSn sample similar to that used in the 2D DIC study was imaged using X-ray microtomography. The cubic sample measured approximately 300 μm on a side, and was imaged with scan parameters similar to those used in the solder joint study with the exception that the glass filter was removed. The sample was imaged and then indented with four ~20 um deep Vickers indentations before reimaging. The 3D models of the joint before (yellow) and after deformation (red) are shown in Figure 22.

Figure 22: 3D model of solder sample before (yellow) and after indentation (red). The circular yellow areas on the top surface correspond with the indentation sites. While the phase spacing is rather large according to the 2D imagery, there is very low contrast between the phases in the lab scale tomography data. Nonetheless, comparison of the same 2D cross section in the before and after deformation data shown in Figure 23.

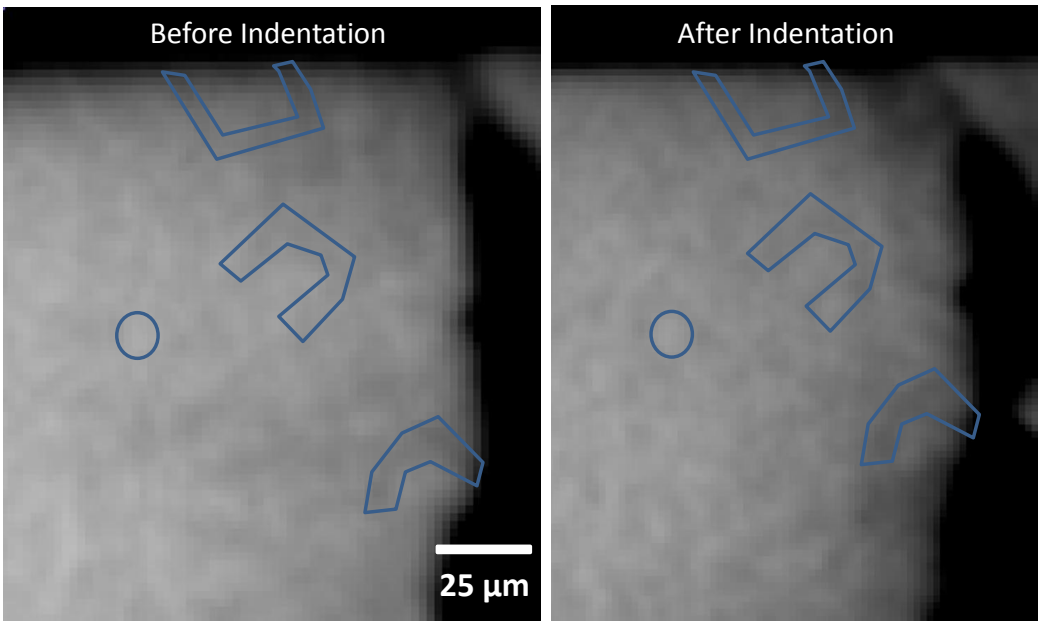

Figure 23: Tomography cross sections through the before and after indentation datasets. Some common features that can be identified in both datasets are outlined in blue.

It is hypothesized that a better dataset for DVC analysis can be obtained using synchrotron tomography, due to higher signal-to- noise ratio and the ability to measure phase contrast. High quality segmentations on this alloy using Synchrotron Tomography data have been obtained by our group. (Yazzie, et al. 2012 (Submitted)) An example of this is shown in Figure 24:

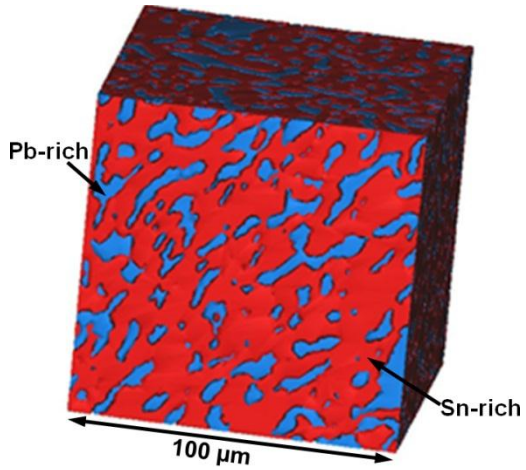

Figure 24: 3D visualization of Sn-37Pb microstructure reconstructed from x-ray tomography data. A cubic volume of material was selected from a region of the Sn-37Pb pillar specimen which had uniform contrast. Morphology of Pb-rich and Sn-rich phases were accurately represented. 3D visualization showed that Sn-rich and Pb-phases were fully interconnected. From (Yazzie, et al. 2012 (Submitted))

While the current study using lab scale tomography has yet to produce high-quality results for DVC, there are improvements that can be made to the imaging process. Phase contrast imaging, a common source of contrast between similar absorption phases in synchrotron tomography data has recently been utilized in lab scale equipment (Kastner, Plank and Requena 2012). It is also possible that higher contrast between phases can be obtained using thinner samples, as well as lower X-ray energies. These and other improvements hold promise for future DVC data being obtained using lab scale microtomography.

Chapter 6

SUMMARY

This concludes the experimental work completed for this thesis. There are several avenues of Future work that would improve on the results obtained here.

The first that has been discussed deals with the segmentation error. In this experiment, the error in particle segmentation was measured using 2D surface measurements. A more thorough experiment would require that 3D phases of a known size are compared to measured volume of the segmented masks. This can be done either by using marker phases that are manufactured to a precise size such as glass microspheres, or by measuring the 3D volume of the phases using a high resolution technique such as FIB tomography. This would produce a more realistic measure of the segmentation error in the experiment.

A second avenue of future work involves improved validation of the Finite Element Model. Completing the Digital Volume Correlation measurements on a 3D dataset would provide an experimentally measured local equivalent strain measurement that could be directly compared with the Finite Element predictions. This will allow fine tuning of the Finite Element model, which could then be tested on other labscale tomography-imaged microstructures.

In addition a useful characterization of the Finite Element model would involve measuring its ability to predict the crack nucleation strain. This measurement would require a series of tomography datasets taken with very small strain increments, and is better suited for an in-situ tomography experiment, rather than the interrupted test conducted here. The resulting data can then be examined

to determine the strain at which the crack becomes large enough to be resolvable in the tomography. Crack initiation could also be studied through other experimental techniques such as acoustic emission.

In this thesis, the study of the deformation and failure of Cu/solder joints was conducted using 3D x-ray tomography. A joint was deformed through a series of loading experiments, and the localized deformation of the pores in the joint was quantified by measuring the changes in pore sphericity. These sphericity measurements were then compared to the predictions of a Finite Element model designed to simulate failure of the joint. The sphericity comparison measurements indicate that the Finite Element Model correctly captures the broad features of deformation, including the strain localization present in the joint. Additionally, comparison of the crack propagation path observed in the experimental data with the model shows very good agreement. Further enhancements of the Finite Element model can be made by comparing the simulated local deformation with the strain plots measured using a Digital Image Correlation technique, and PbSn was shown to have microstructural features that are sufficient to perform 2D based DIC measurements.

REFERENCES

Aspandiar, R. *Voids in Solder Joints.* Northwest Chapter Meeting, Septemeber: Technical Report,Intel Corporation, 2005.

Baruchel, J, et al. "Advances in synchrotron hard X-ray based imaging." *Comptes Rendus Physique* 9, no. 5-6 (2008): 624-641.

Baruchel, J, et al. "Advances in synchrotron radiation microtomography." *Script Mater* 55 (2006): 41-46.

Cao, S, S Pourbabak, and D. Schryvers. "Quantitative 3-D morphologic and distributional study of Ni4Ti3 precipitated in a Ni51Ti49 single cystal alloy." *Scripta Materialia* 66 (2012): 650-653.

Chawla, N, and X Deng. "Microstructure and mechanical behavior of porous sintered steels." *Materials Science and Engineering A* 390 (2005): 98-112.

Chawla, N, J J Williams, X Deng, C McLimon, L Hunter, and S H Lau. "Three Dimensional (3D) characterization and Modeling of Porosity in Power Metallurgy (P/M) Steels." *Int J Power Met* 45, no. 2 (2009): 19-28.

Chawla, N, R Sidhu, and V Ganesh. "Three-dimensional Visualization and microstructure-based modeling of deformation in particle-reinforced composites." *Acta Materialia* 54 (2006): 1541-1548.

Chiang, YC, P Rosch, A Dabanoglu, and CP Lin. "Polymerization composite shrinkage evaluation with 3D deformation analysis from µCT images." *Dental Materials* 26 (2010): 223-231.

Dassault Systems Simulia Corp, D. "Abaqus 6.9 User's Manual." Providence, RI, 2010.

Dudek, M, and N Chawla. "Three-dimensional (3D) Microstructure Visualization of LaSn3 Intermetallics in a Novel Sn-rich Rare-earth-containing Solder." (Materials Characterization) 59, no. 9 (2008): 1364-1368.

Dudek, M, L Hunter, JJ Williams, H Lau, S Kranz, and N Chawla. "Three dimensional visualization of reflow porosity and modeling of deformation in Pb-free solder joints." *Materials Characterization* 61 (2010): 433-439.

Falcao, AX, JK Udupa, S Samarasekera, S Sharma, BE Hirsch, and RA Lotufo. "User-steered image segmentation paradigms: Live-wire and live-lane." *Graph Model Image Process* 60, no. 4 (1998): 233-260.

Felberbaum, M, and M Rappaz. "Curvature of micropores in Al-Cu alloys: An X-ray tomography study." *Acta Materialia* (Elsevier Ltd.) 59 (2011): 6849-6860.

Gao, YX, JZ Yi, PD Lee, and TC Lindley. "A micro-cell model of the effect of microstructure and on fatugue resistance in cast Al alloys." *Acta Mater* 52 (2004): 5435-5449.

Gao, YX, JZ Yi, PD Lee, and TC Lindley. "The Effect of porosity on the fatigue life of cast aluminum-silicon alloys." *Fatigue Fract Eng Mater Struct* 27 (2004): 559-570.

Guide, Mimics 13.1 Reference. n.d.

Haldrup, K, SF Nielsen, F Beckmann, and JA Wert. "Plastic Strain measurements: from 2D to 3D." *Materials Science and Technology* 21 (2005): 1428-1431.

Jiang, L, N Chawla, M Pacheco, and V. Noveski. "Three-Dimensional (3D) microstructural characterization and quantification of reflow porosity in Sn-rich alloy/copper joints by x-ray tomography." *Materials Characterization* 62 (2011): 970-975.

Kastner, J, B Plank, and G Requena. "Non-destructive characterisation of polymers and Al-alloys by polychromatic cone-beam phase contrast tomography." *Materials Characterization* 64 (2012): 79-87.

Kinney, JH, and MC Nichols. "X-ray tomographic microscopy (XTM) using synchrotron radiation." *Annual Review of Materials Science* 22, no. 1 (1992): 121-152.

Kobayashi, M, et al. "High-Density three-dimensional mapping of internal strain by tracking microstructural features." *Acta Materialia* 56 (2008): 2167-2181.

Kubis, AJ, GJ Shiflet, and R Hull. "Focused Ion Beam Tomography." *Metallurgical and Materials Transaction A* 35, no. 7 (2004): 1935-1943.

Ladani, L, and A Dasgupta. "Effect of Voids on Thermo-Mechanical Durability of Pb-free BGA solder Joints: Modeling and Experiment." (Journal of Electronic Packaging) 129 (2007): 273-278.

Landron, C., E. Maire, O. Bouaziz, J. Adrien, L. Lecarme, and A. Bareggi. "Validation of void growth models using X-ray microtomography characterization of damage in dual phase steels." *Acta Materialia* 59 (2011): 7564-7573.

Lange, D, H. M. Jennings, and S. P. Shah. "Image analysis Techniques for characterization of pore structure of cement-based materials." *Cement and Concrete Research* 24, no. 5 (1994): 841-853.

Lasagni, F, A Lasagni, E Marks, C Holzapfel, F Muchlich, and HP Degischer. "Three-dimensional characterization of 'as-cast' and solution-treated AlSil2(Sr) alloys by high resolution FIB tomography." *Acta Mater* 55 (2007): 3875-3882.

Lau, J, and S Eramus. "Effects of Voids on Bump Chip Carrier (BCC++) Solder Joint Reliability." San Diego: IEEE Electronic Components and Technology Conference, 2002. 992-998.

Lee, T, J Lee, and I. Jung. "Finite element analysis for solder ball failures in chip scale package." *Microelectronics and Reliability* 38, no. 12 (1998): 1941-1947.

Li, P, PD Lee, TC Linsey, DM Maijer, GR Davis, and JC. Elliott. "X-ray Microtomographic Characterisation of Porosity and its Influence of Fatigue Crack Growth." *Adv Eng Mater* 8 (2006): 476-479.

Link, T, S Zabler, A Epishin, M Bansal, and X Thibault. "Synchrotron tomography of porosity in single-crystal nickel-base superalloys." *Materials Science and Engineering A* (Elsevier B.V.) 425 (2006): 47-54.

Maire, E., S. Zhou, J. Adrien, and M. Dimichiel. "Damage quantification in aluminium alloys using in situ tensile teste in X-ray tomography." *Engineering Fracture Mechanics* 78 (2011): 2679-2690.

Martin, C.F., C. Josserond, L. Salvo, J.J. Blandin, P. Cloetens, and E Boller. "Characterisation By X-ray Micro-tomography of cavity coalescence during superplastic deformation." *Scripta Mater.* 42 (2000): 375-381.

Mortensen, EN, and WA. Barrett. "Interactive Live-Wire Boundary Extraction." *Med Image Anal* 1, no. 4 (1997): 331-341.

Mortensen, EN, and WA. Barrett. "Interactive Segmentation with Intelligent Scissors." *Graph Model Image Process* 60 (1998): 349-384.

Nakazawa, M, Y Aoki, H Toda, and M Kobayashi. "3D Image Analysis for Evaluating Internal Deformation/ Fracture Characteristics of Materials." *Electronics and Communications in Japan* 91, no. 12 (2008): 16-23.

Nicoletto, G, R Konecnia, and S. Fintova. "Characterization of microshinkage casting defects of Al-Si alloys by X-ray computer tomography and metallography." *Int J Fatigue*, 2012 (in press).

Nielsen, SF, HF, Beckmann, F Poulsen, C Thorning, and JA Wert. "Measurements of plastic displacement gradient components in three dimensions using marker particles and synchrotron X-ray absorption microtomography." *Acta Materialia* 51 (2003): 2407-2415.

Pacheco, M, and D. Goyal. "New Developments in High Resolution X-ray Computed Tomograpphy for Non-Destructive Defect Detection in Next Generation Package Technologies." *ISTFA.* 2008. 30-35.

Padilla, E, V Jakkali, L Jiang, and N Chawla. "Quantifying the Effect of Porosity on the Evolution of Deformation and Damage in Sn-based Solder Joints by X-ray Microtomography and Microstructure-based Finite Element Modeling ." *Acta Materialia,* In Press.

Personal Correspondence with D. Beski, Materialise. 2012.

Plieninger, R., M. Dittes, and K. Pressel. "Modern IC Packaging Trends and their Reliability Implications." *Microelectronics Reliability* 46 (2006): 1868-1873.

Poon, M, G Hamarneh, and R. Abugharbieh. "Efficeint interactive 3D Livewire segmentation of complex objects with arbitrary topology." *Comput Med Imaging Graph* 32 (2008): 639-650.

Shen, H, and LC Brinson. "Finite element modeling of porous titanium." *Int J Solids Struct* 44 (2007): 320-335.

Shen, YL, N Chawla, E Ege, and X Deng. "Deformation analysis of lap-shear testing of solder joints." *Acta Materialia* 53 (2005): 2633-2642.

Sindhu, RS., and N. Chawla. "Three Dimensional Microstructure Characterization of Ag3Sn Intermetallics in Sn-rich solder by serial sectioning." *Materials Characterization* 52, no. 3 (2004).

Singh, DRP, and N Chawla. "Focused Ion Beam (FIB) tomography of nanoindentation damage in nanoscale metal/ceramic multilayers." *Materials Characterization* 61, no. 4 (2010): 481-488.

Stock, SR. "Recent advances in x-ray microtomography applied to materials." *Int Mater Rev* 53, no. 3 (2008): 129-181.

Tanie, T, and H Terasaki. "Fatigue Crack Propagation Analysis for Micro Solder Joints with Void." International Symposium on Electronics Materials and Packaging, 2005.

Tian, T, K Chen, A. A. MacDowell, D. Lai, YS Parkinson, and K.N. Tu. "Quantitative X-ray microtomography study of 3-D void growth induced by electromigration in eutectic SnPb flip-chip solder joints." *Scripta Materialia* 65 (2011): 646-649.

Toda, H, E Maire, Y Aoki, and M. Kobayashi. "Three-dimensional strain mapping using in situ X-ray synchrotron microtomography." *J. Strain Analysis* 46 (2011).

Vanderesse, N, Mairen E, A Chabod, and JY. Buffiere. "Microtomographic study and finite element analysis of the porosity harmfulness in a cast aluminium alloy." *Int J of Fatigue* 33 (2011): 1514-1525.

Wang, Y, F Duewer, S Kamath, D Scott, and W Yun. "A Novel X-ray Microtomography System with High Resolution and Throughput." *NSTI Nanotechnol Conf Trade Show Nanotech* 3 (2004): 503-507.

Weck, A, DS Wilkinson, E Maire, and H Toda. "Visualization by X-ray tomography of void growth and coalescence leading to fracture in model materials." *Acta Mater* 56 (2008): 2919-2928.

Weiler, J.P., J.T. Wood, R.J. Klassen, E Maire, R Berkmortel, and G Wang. "Relationship between internal porosity and fracture strength of die-cast magnesium AM60B alloy." *Materials Science and Engineering A* (Elsevier B.V.) 395 (2005): 315-322.

Xu, Z, W Wen, and T Zhai. "Effects of Pore Position in Dept on Stress/Strain Concentration and Fatigue Crack Initiation." *Metall Mater Trans A*, 2011.

Yazzie, K.E., J.J. Williams, N.C. Phillips, F De Carlo, and N. Chawla. "Characterization of Intermetallic Precipitates and Contiguous Phases in Sn-rich Alloys Using 3D X-ray Synchrotron Tomography." *Materials Characterization*, 2012 (Submitted).

Youssef, S, E Maire, and R Gaertner. "Finite Element modeling of the actual structure of cellular materials determined by X-ray tomography." *Acta Mater* 53 (2005): 719-730.

Yu, Q, T Shibutani, D Kim, Y Kobayashi, and J Yang. "Effect of process-induced voids on isothermal fatigue resistance of CSP Lead Free Solder Joints." *Microelectronics Reliability* 48 (2008): 431-437.

Yunus, M, K Srihari, J Pitaressi, and A Primavera. "Effect of voids on the reliability of BGA/CSP solder joints." *Microelectronics Reliability* 43 (2003): 2077-2086.

Zhu, N. Annual IEEE Semiconductor Thermal Measurement Management Symposium, 1999. 22-29.